Orbital forcing, ice-volume and CO_2 across the Oligocene-Miocene Transition

Rosanna Greenop[1, 2], Sindia M. Sosdian[3], Michael J. Henehan[4], Paul A. Wilson[1], Caroline H. Lear[3] and Gavin L. Foster[1]

[1] School of Ocean and Earth Science, National Oceanography Centre Southampton, University of Southampton Waterfront Campus, European Way, Southampton, SO14 3ZH, UK.
[2] School of Earth and Environmental Science, Irvine Building, University of St Andrews, North Street, St Andrews, KY16 9AL, UK.
[3] School of Earth and Ocean Sciences, Cardiff University, Main Building, Park Place, Cardiff, CF10 3AT.
[4] GFZ German Research Centre for Geosciences, Telegrafenberg, 14473, Potsdam, Germany

Keywords

OMT, Miocene, CO_2, Antarctica, cryosphere, boron isotopes

Key points

- CO_2 levels were relatively low (~265 ppm; $2\sigma\ ^{+166}_{-111}$ ppm) and comparatively stable in the 500 kyrs prior to and during the glaciation.
- CO_2 increased by ~65 ppm during the OMT deglaciation consistent with the latest generation of ice sheet models.
- The timing of the OMT glaciation is most likely controlled by both changes in CO_2 and favourable orbital forcing.

Abstract

Paleoclimate records suggest that a rapid major transient Antarctic glaciation occurred across the Oligocene-Miocene transition (OMT; ca. 23 Ma; ~50 m sea level equivalent in 200-300 kyrs). Orbital forcing has long been cited as an important factor determining the timing of the OMT glacial event. A similar orbital configuration occurred 1.2 million years prior to the OMT, however, and was not associated with a major climate event, suggesting that additional mechanisms play an important role in ice sheet growth and decay. To improve our understanding of the OMT, we present a boron isotope-based CO_2 record between 22 and 24 Ma. This new record shows that $\delta^{11}B/CO_2$ was comparatively stable in the million years prior to the OMT glaciation and decreased by 0.7 ‰ (equivalent to a CO_2 increase of ~65 ppm) over ~300 kyrs during the subsequent deglaciation. More data are needed but we propose that the OMT glaciation was triggered by the same forces that initiated sustained Antarctic glaciation at the Eocene-Oligocene transition; long-term decline in CO_2 to a critical threshold and a superimposed orbital configuration favourable to glaciation (an eccentricity minimum and low-amplitude obliquity change). When comparing the reconstructed CO_2 increase with estimates of $\delta^{18}O_{sw}$ during the deglaciation phase of the OMT, we find that the sensitivity of the cryosphere to CO_2 forcing is consistent with recent ice sheet modelling studies that incorporate retreat into subglacial basins via ice cliff collapse with modest CO_2 increase, with clear implications for future sea level rise.

1. Introduction

Over the last 55 million years Earth's climate has gradually cooled but superimposed upon this long-term evolution are numerous intervals of more rapid change (Zachos et al., 2008). One such example of rapid change is the glaciation that coincides with the Oligocene-Miocene stratigraphic boundary (terminology of Miller et al., 1991; ca. 23 Ma, see Fig. 1). This transient cooling event is evident in the oxygen isotope record as a two-step increase in benthic foraminiferal $\delta^{18}O$ over 200-300 thousand years. The magnitude of this change has typically been estimated to be approximately 1 ‰, and interpreted to represent a temporary expansion in continental ice volume of between 30 and 90 m sea level equivalent (s.l.e) (Liebrand et al., 2011; Mawbey and Lear, 2013; Miller et al., 1991; Pälike et al., 2006a; Pälike et al., 2006b; Paul et al., 2000; Pekar et al., 2002). However, a recent re-evaluation of stacked benthic $\delta^{18}O$ records (Mudelsee et al., 2014), alongside a new oxygen isotope record from IODP Site U1334 in the equatorial Pacific (Beddow et al., 2016), suggests that the excursion is smaller (~ 0.6 ‰) and that previous work placed too much emphasis on the extremes in the interpretation of the individual records published across the interval. Assuming the same $\delta^{18}O$ to sea level relationship as the late Pleistocene, the re-evaluation of the oxygen isotope excursion suggests a sea level change of up to ~50 m (Beddow et al., 2016). Previous work has suggested $\delta^{18}O_{ice}$ may be less enriched in ^{16}O when ice sheets are smaller (e.g. Langebroek et al., 2010), which would lead to an increase in the sea level change inferred from a $\delta^{18}O_{sw}$ excursion (e.g. Edgar et al., 2007), however, this effect is likely to be a relatively minor component (15-28%) of the total $\delta^{18}O$ change during the Neogene (Gasson et al., 2016a; Gasson et al., 2016b; Langebroek et al., 2010). Slightly higher ice volume changes are estimated in a study by Liebrand et al., (2017), which uses the benthic $\delta^{18}O$ record from Site 1264 and assumptions about bottom water temperature. That study estimates that the OMT was associated with a change in the East Antarctic ice sheet from near-fully deglaciated to one as large as the modern day. While it is not possible to discount a northern hemisphere contribution to the continental ice budget of the OMT, despite the uncertainties in total ice volume change, Antarctica is likely to have been the main locus of ice growth at this time (DeConto et al., 2008; Naish et al., 2001).

Existing studies have shown that orbital forcing plays a key role in OMT glaciation because its timing is closely associated with the 1.2 Myr minimum in the modulation of the Earth's orbit and axial tilt (an obliquity 'node'), as well as a minimum in the 400 kyr long eccentricity cycle (i.e. a very circular orbit), both of which reduce seasonal extremes and increase the chances of winter snowfall surviving the summer ablation season (Coxall et al., 2005; Pälike et al., 2006a; Zachos et al., 2001b) (Fig. 1). However, obliquity nodes and eccentricity minima occur regularly throughout the late Oligocene (Laskar et al., 2004) and the amplitude of the preceding node at 24.4 Ma is more extreme than the one associated with the Oligocene-Miocene transition (Pälike et al., 2006a). Consequently, despite a clear orbital pacing to the OMT glaciation, changes in other boundary conditions are required to fully explain this climate perturbation (Liebrand et al., 2017).

Records of deep-ocean cooling and ice sheet expansion/retreat associated with the OMT glaciation exhibit a number of orbitally paced steps (Lear et al., 2004; Liebrand et al., 2011; Liebrand et al., 2017; Mawbey and Lear, 2013; Naish et al., 2001; Pälike et al., 2006a; Pälike et al., 2006b; Zachos et al., 2001b). There is a □100 kyr periodicity throughout the OMT in a number of benthic oxygen isotope records, as well as in $\delta^{18}O_{sw}$ (calculated from paired benthic $\delta^{18}O$ and Mg/Ca measurements), which is expressed particularly clearly following the main glaciation (Beddow et al., 2016; Liebrand et al., 2011; Mawbey and Lear, 2013; Zachos et al., 2001b). Statistical analysis of the benthic $\delta^{18}O$ record from ODP Site 1264 across the Oligocene-Miocene suggests that the symmetry of □100 ky glacial-interglacial cycles changes across the OMT with a switch to more asymmetric cycles, indicative of longer-lived ice sheets that survive deeper into insolation maxima (increased ice sheet hysteresis) together with more abrupt glacial terminations after □23 Ma (Liebrand et al., 2017).

It has also been suggested that OMT glaciation was associated with a perturbation of the carbon cycle (Mawbey and Lear, 2013; Paul et al., 2000; Zachos et al., 1997). Modelling studies (DeConto and Pollard, 2003; Gasson et al., 2012) and proxy reconstructions (e.g. Foster et al., 2012; Foster and Rohling, 2013; Greenop et al., 2014; Martínez-Botí et al., 2015; Pagani et al., 2011; Pearson et al., 2009) both suggest that CO_2 plays an important role in controlling the timing of ice sheet expansion and retreat throughout the Cenozoic. The long-term increase of 0.8‰ in carbon isotopes from 24 to 22.9 Ma, alongside an increase in benthic foraminiferal U/Ca has been attributed to an increase in global organic carbon burial and the associated reduction in atmospheric CO_2 (Fig. 1) (Mawbey and Lear, 2013; Paul et al., 2000; Stewart et al., 2017; Zachos et al., 1997). On the basis of deep-ocean $CaCO_3$ preservation indicators and estimates of deep-ocean CO_3^{2-}, an increase in CO_2 has also been implicated as one of the driving forces of the deglaciation that followed the glacial maximum at 23 Ma (Mawbey and Lear, 2013). Yet, published CO_2 records are not of sufficient temporal resolution to test these hypotheses or evaluate the presence of a CO_2 decline that would be expected to accompany an increase in organic carbon burial prior to OMT glaciation (Fig. 1).

The overall OMT glaciation-deglaciation event as seen in the $\delta^{18}O$ record shows a duration of about one million years and is largely symmetrical, with little evidence of ice sheet hysteresis (Beddow et al., 2016; Liebrand et al., 2011; Mawbey and Lear, 2013; Zachos et al., 2001b). While the first generation of Antarctic ice sheet models suggested that the CO_2 threshold for retreat of a major ice sheet was high (>1000 ppm) (Pollard and DeConto, 2005), more recent studies suggest that it is possible to simulate a more dynamic ice sheet by (i) incorporating an atmospheric component to the model to account for ice sheet–climate feedbacks, (ii) allowing for ice sheet retreat into subglacial basins via ice cliff collapse and, (iii) accounting for changes in the oxygen isotope composition of the ice-sheet (Gasson et al., 2016b; Pollard et al., 2015). Based on modelling experiments for the early to mid-Miocene Antarctic ice sheet, a seawater oxygen isotope change of 0.52-0.66 ‰, can be simulated by changing atmospheric CO_2 between 280 and 500 ppm together with applying an astronomical configuration favorable for Antarctic deglaciation (Gasson et al., 2016b). To assess the controls on ice sheet dynamics and the potential applicability of this new generation of ice sheet models to the OMT glaciation, CO_2 data are required at substantially higher resolution than is currently available (1 sample per ~500 kyr; Fig 1). Here, we present a new boron isotope record with an average 50 kyr resolution across the OMT glaciation and use published $\delta^{18}O$ records to explore the relationship between ice volume and CO_2 across this interval.

2. Methods and Site information

2.1 Site Location and Information:

We utilize sediments from two open ocean drill site holes: Ocean Drilling Program (ODP) Hole 926B from Ceara Rise (3°43′N, 42°54′W; 3598 m water depth) in the Equatorial Atlantic Ocean and ODP Hole 872C situated in the tropical north Pacific gyre on the sedimentary cap of a flat-topped seamount (10°05.62'N, 162°52.002'E, water depth of 1082 m). Both sites are currently located in regions where surface water is close to equilibrium (+/- 25 ppm) with the atmosphere with respect to CO_2 (Fig. 2; (Takahashi et al., 2009)). Age models for Site 926 and Site 872 are from Pälike et al., (2006a) (and references therein) and Sosdian et al., (2018) updated to GTS2012 (Gradstein et al., 2012) respectively. Samples from ODP Site 926 were taken from between 469 and 522 mcd and between 110 and 117 mcd at ODP Site 872.

2.2 Boron isotope measurements

Trace element and boron isotope (described in delta notation as $\delta^{11}B$ – permil variation from the boric acid standard SRM 951; Catanzaro et al., 1970) measurements were made on the $CaCO_3$ shells of the mixed-layer dwelling foraminifera *Globigerina praebulloides* (250-300 μm) at Site 926. At Site 872, mixed layer dwelling foraminifera *Trilobatus trilobus* (300-355 μm) was analysed. The foraminifera were cleaned following the oxidative cleaning methodology of Barker et al., (2003) before dissolution by incremental addition of 0.5 M HNO_3. Trace element analysis was then conducted on a small aliquot of the dissolved sample at the University of Southampton using a ThermoFisher Scientific Element XR to measure Mg/Ca for ocean temperature estimates and Al/Ca to assess the competency of the sample cleaning. For boron isotope analysis the boron was first separated from the Ca (and other trace elements) matrix using the boron specific resin Amberlite IRA 743 (Foster, 2008; Foster et al., 2013). The boron isotopic composition was then determined using a sample-standard bracketing routine on a ThermoFisher Scientific Neptune multicollector inductively coupled plasma mass spectrometer (MC-ICPMS) at the University of Southampton (closely following Foster et al., 2013). The uncertainty in $\delta^{11}B$ is determined from the long-term reproducibility of Japanese Geological Survey Porites coral standard following Greenop et al., (2017).

2.3 Determining pH from $\delta^{11}B$

The relationship between $\delta^{11}B_{calcite}$ and pH is very closely approximated by the following equation:

$$pH = pK_B^* - \log\left(-\frac{\delta^{11}B_{SW} - \delta^{11}B_{calcite}}{\delta^{11}B_{SW} - \alpha_B.\delta^{11}B_{calcite} - 1000.(\alpha_B - 1)}\right) \quad (1)$$

where pK_B^* is the equilibrium constant, dependent on salinity, pressure, temperature and seawater major ion composition (i.e. $[Ca]_{sw}$ and $[Mg]_{sw}$), α_B is the fractionation factor between the two boron species (1.0272; Klochko et al., 2006) and $\delta^{11}B_{sw}$ is the boron isotope composition of seawater. In the absence of changes in the local hydrography, variations of atmospheric CO_2 have a dominant influence on pH and $[CO_2]_{aq}$ in the surface water.

2.3.1 Vital effects

Although the $\delta^{11}B$ of foraminifera correlates well with pH and $[CO_2]_{aq}$ the $\delta^{11}B_{calcite}$ is often not exactly equal to $\delta^{11}B_{borate}$ (e.g. Foster, 2008; Henehan et al., 2013; Sanyal et al., 2001). For instance, while the pH sensitivity of $\delta^{11}B$ in modern *G.bulloides* is similar to the pH sensitivity of $\delta^{11}B$ in borate ion, the relationship between pH and $\delta^{11}B$ falls below the theoretical $\delta^{11}B_{borate}$-pH line (Martínez-Botí et al., 2015) (i.e a lower $\delta^{11}B$ for a given pH). This effect has been attributed to the dominance, in this asymbiotic foraminifer, of respiration and calcification on the foraminifer's microenvironment, which both act to drive down local pH (Hönisch et al., 2003; Zeebe et al., 2003). In contrast, photosynthetic processes in symbiont-bearing foraminifera can cause the pH of the micro-environment to be elevated above that of the ambient seawater (Henehan et al., 2013) and the magnitude of the pH elevation determines the offset between $\delta^{11}B_{borate}$ and $\delta^{11}B_{calcite}$, which is expressed in a species-specific calibration (Henehan et al., 2016; Hönisch et al., 2003; Zeebe et al., 2003). In order to use modern calibrations further back in time, when the foraminifera were growing under different $\delta^{11}B_{sw}$, it is necessary to also correct the calibration for the $\delta^{11}B_{sw}$ to avoid overcorrecting for vital effects (see Supp. Fig. 1, 2). Here we adjust the modern calibration intercept using:

$$c_{\delta^{11}B_{sw}} = c_0 + \Delta\delta^{11}B_{sw}(m_0 - 1) \quad (2)$$

where c_0 and m_0 are the intercept and slope of the calibration at modern $\delta^{11}B_{sw}$ and $\Delta\delta^{11}B_{sw}$ is the difference in $\delta^{11}B_{sw}$ between modern $\delta^{11}B_{sw}$ and the $\delta^{11}B_{sw}$ of interest (calculated from the mid-point in the OMT $\delta^{11}B_{sw}$ range; see below). Using the calibration corrected for OMT $\delta^{11}B_{sw}$ leads to a marginally higher calculated $\delta^{11}B_{borate}$ (~0.25 ‰ and hence lower pCO_2) compared to the modern calibration.

At Site 872 we measure *T. trilobus* from the 300-350µm size fraction and use the calibration of Sanyal et al., (2001) with a modified intercept so that it passes through the core top value for the related *T. sacculifer* (300–355 µm) from ODP 999A (Seki et al., 2010) to correct for vital effects (Sosdian et al., 2018):

$\delta^{11}B_{borate}$= ($\delta^{11}B_{T.trilobus}$-2.69)/0.833 (3)

At Site 926 *G. praebulloides* was measured from the 250-300 µm size fraction. Studies based on the change in $\delta^{13}C$ and $\delta^{18}O$ with size fraction have shown that at the Oligocene-Miocene transition *G. praebulloides* appears to be symbiotic (Pearson and Wade, 2009), in contrast to the asymbiotic modern *G. bulloides* that is considered to be its nearest living relative. Consequently the modern $\delta^{11}B$-pH calibration of *G. bulloides* (Martínez-Botí et al., 2015) is not applicable. Instead we use the calibration for the symbiotic foraminifera *T. sacculifer*. In the absence of a *T. sacculifer* calibration for the 250-300 µm size fraction, we apply the same calibration as at Site 872 from Sosdian et al., (2018). We then use the close temporal overlap between the data from our two sites and with the different species to examine the validity of these vital effect assumptions.

2.3.2 Parameters for calculating pK_B^*

Temperature changes across the Miocene-Oligocene boundary are assessed here using Mg/Ca derived temperatures. SSTs are calculated from tandem Mg/Ca analyses using the generic Mg/Ca temperature calibration of Anand et al., (2003). Adjustments were made for changes in Mg/Ca_{sw} using the records of Brennan et al., (2013) and Horita et al., (2002) and correcting for changes in dependence on Mg/Ca_{sw} following Evans and Muller, (2012) using H = 0.42 calculated from *T. sacculifer* (Delany et al., 1985; Evans and Muller, 2012; Hasiuk and Lohmann, 2010). We apply a conservative estimate of uncertainty in Mg/Ca-SST of ± 3ºC (2σ), to account for analytical and calibration uncertainty, as well as uncertainty in the magnitude of the Mg/Ca_{sw} correction. The temperature effect on CO_2 calculated from $\delta^{11}B$ is ~ 10-15 ppm/ºC, consequently uncertainty in SSTs does not significantly contribute to the final pH and CO_2 uncertainty. We assume salinity values of the same as modern day at both sites and apply a conservative estimate of ± 3 psu to account for any changes in this parameter through time. Salinity has little effect on CO_2 uncertainty calculated using $\delta^{11}B$ (± 3-14 ppm for a ± 3 ‰). We use the MyAMI Specific Ion Interaction Model (Hain et al., 2015) to adjust pK^*_B for changing Mg/Ca_{sw} based on the $[Mg]_{sw}$ and $[Ca]_{sw}$ reconstructions of Brennan et al., (2013) and Horita et al., (2002) (Supp. Fig. 3).

2.3.3 The boron isotopic composition of seawater ($\delta^{11}B_{sw}$)

The long residence time of boron in the oceans (~ 10 to 20 Myrs) ensures that major changes in $\delta^{11}B_{sw}$ during our 2 Myr-long study interval are unlikely (Lemarchand et al., 2000) but it is probable that $\delta^{11}B_{sw}$ has shifted from its present value of 39.61 ‰ over the past 24 million years. The $\delta^{11}B_{sw}$ during the Oligo-Miocene is therefore a large source of uncertainty and can have a significant effect on the absolute CO_2. For instance, Greenop et al., (2017) showed that the various records of $\delta^{11}B_{sw}$ diverge significantly in the early Miocene leading to large uncertainties in absolute CO_2 estimates across this interval (Sosdian et al., 2018). Here we apply a flat probability for $\delta^{11}B_{sw}$ in the range of 37.17 to 39.73‰ to encompass the different estimates. The minimum of this range is set to the lower 1σ uncertainty of the smoothed Greenop et al., (2017) record between 22.6 and 23.1 Ma calculated from paired planktic-benthic foraminiferal $\delta^{11}B$ and $\delta^{13}C$ analyses. The maximum extent is the average upper 1σ uncertainty of the $\delta^{11}B_{sw}$ estimates between 21.7 Ma and 24.4 Ma from Raitzsch and Hönisch, (2013) calculated from the $\delta^{11}B$ of benthic foraminifera, coupled to assumptions in past changes in CO_2, using a $\propto_B$ of 1.0272 (Klochko et al., 2006). This range also encompasses the geochemical modeling estimates of $\delta^{11}B_{sw}$ from Lemarchand et al., (2000) and estimates based on the non-linear relationship between $\delta^{11}B$ and pH alongside estimates of surface to thermocline pH gradients (Palmer et al., 1998; Pearson and Palmer, 2000) from the same time interval (Supp. Fig. 3).

2.4 Estimating absolute CO_2

To define atmospheric CO_2, a second carbonate system parameter, in addition to pH, is required. We use the regression of the Neogene DIC estimates from Sosdian et al., (2018), where deep-ocean DIC is calculated from benthic $\delta^{11}B$ derived estimates of bottom water pH and deep-ocean carbonate ion concentration ($[CO_3^{2-}]$) constrained by the calcite compensation depth (CCD) and $[Ca]_{sw}$. A linear regression is fitted through the deep-ocean DIC estimates and used to estimate changes in surface DIC relative to the modern value of 2000µmol/kg (Supp. Fig. 3). The major source of uncertainty in the DIC estimates is the $\delta^{11}B_{sw}$ record used to calculate bottom water pH (Sosdian et al., 2018). For instance, the three $\delta^{11}B_{sw}$ record used in Sosdian et al., (2018) results in a wide range of calculated DIC estimates (e.g. 1430 to 1940 µmol/kg at 21.2 Ma). Consequently to incorporate this uncertainty we calculate absolute CO_2 using the DIC regressions determined from the three $\delta^{11}B_{sw}$ records (Sosdian et al., 2018). We undertake a full error propagation of CO_2 using a Monte Carlo simulation (n=10000) by perturbing each data point within the 2σ uncertainty limits in the $\delta^{11}B$ measurement (± 0.16-0.85 ‰), SST (± 3 ºC), SSS (± 3 psu), $\delta^{11}B$ seawater (flat probability estimate between 37.15 to 39.51‰) and DIC (±378-502 µmol/kg). We then combine all the Monte Carlo simulations of CO_2 calculated using the three different DIC regressions (n=30000) to determine the mean and 2σ of the final CO_2 estimate (Supp. Fig. 4). By using this approach the final CO_2 estimate (and associated uncertainty) reflects the full spread of DIC estimates while utilizing the overlap in the DIC estimates calculated using different $\delta^{11}B_{sw}$ records to increase the certainty in our CO_2 estimates. This approach results in a slight decrease in the 2σ uncertainty of the combined simulations (n=30000) when compared to the values obtained when using each DIC estimate in isolation. All carbonate system equilibrium constants are corrected for changes in Mg/Ca_{sw} based on the $[Mg]_{sw}$ and $[Ca]_{sw}$ reconstructions of Brennan et al., (2013) and Horita et al., (2002) (Supp. Fig. 3) following Hain et al., (2015).

2.5 Estimating relative climate forcing

On timescales of less than a few million years, the close relationship between pH and atmospheric CO_2 forcing means that relative pH (ΔpH) can be used to determine the relative climate forcing from CO_2 change (ΔF_{CO2}; see Hain et al. (2018) for a full discussion). The estimates of $\delta^{11}B$ seawater, DIC, SSTs, SSSs and the $\delta^{11}B$ measurements (and the associated uncertainties) used in the calculation are the same as in Sections 2.3-2.4, however, in analysing ΔF_{CO2} rather than absolute CO_2 forcing the uncertainty in the $\delta^{11}B_{sw}$ and secondary carbonate system parameter become less significant with the primary source of uncertainty originating from the $\delta^{11}B_{calcite}$ measurements (Hain et al., 2018).

ΔF_{CO2} is calculated from ΔCO_2 change using the equation:

$$\Delta F_{CO2} = 5.32 \ln\left(\frac{C}{C_0}\right) + 0.39(\ln\left(\frac{C}{C_0}\right))^2 \quad (4)$$

where C and C_0 are the calculated CO_2 values (Byrne and Goldblatt, 2014). Here C_0 corresponds to the oldest sample at 24.02 Ma and the climate forcing is calculated for the rest of the record relative to this point.

3. Results and Discussion

3.1 $\delta^{11}B$ and temperature changes across the Oligocene-Miocene transition

Our record from *G. praebulloides* at Site 926 shows high and relatively stable $\delta^{11}B$ values (17.1+/- 0.4 ‰; hence lowest CO_2) prior to and during the OMT glaciation (Fig. 3). After 23 Ma, $\delta^{11}B$ decreases in a number of cycles reaching minimum values of 16.3+/- 0.5 ‰ at 22.5 Ma (highest CO_2). The data from Site 872 extends the record from Site 926 between 21-22 Ma and while the samples from the two sites do not overlap in the time domain there appears to be good consistency with the data from Site 926, adding confidence to our treatment of vital effects for *G. praebulloides* at Site 926 (Fig. 3). When comparing the benthic foraminiferal $\delta^{18}O$ record to our $\delta^{11}B$ data, there appears to be a decoupling between the two series in the lead up to the glaciation (Fig. 3). The $\delta^{11}B$ record during this interval shows little change, whereas the $\delta^{18}O$ increases by ~ 0.6 ‰ between 23.2-23.1 Ma. During the deglaciation phase, however, the $\delta^{11}B$ rise broadly tracks the decrease in $\delta^{18}O$ although the $\delta^{11}B$ record shows a transient increase to pre OMT glaciation levels around 22.8 Ma that is less pronounced in the $\delta^{18}O$ record. The $\delta^{11}B$ data from Site 872 suggest that elevated CO_2 levels are only maintained until ~22.2 Ma, after which CO_2 returns to approximately pre-OMT event values. More data are needed to determine whether the $\delta^{11}B$ change between 22.2 Ma to 22 Ma reflects a trend in CO_2 or whether orbital-scale variations have been under-sampled across this interval.

It has been widely hypothesised that a decrease in CO_2 prior to the OMT glaciation may have been one of the key triggers of the event (Mawbey and Lear, 2013; Paul et al., 2000; Zachos et al., 1997). Yet, we find no evidence, within the resolution of our data, for a $\delta^{11}B$ increase (CO_2 decrease) across the benthic $\delta^{13}C$ increase that has been suggested to signify organic carbon burial in the lead-up to the OMT glaciation (Paul et al., 2000; Zachos et al., 1997). That said, the relationship between CO_2 and positive benthic $\delta^{13}C$ excursions is not always straightforward. For example, a $\delta^{13}C$ increase during the warming into the Miocene Climate Optimum coincides with a well-documented CO_2 increase (Foster et al., 2012; Greenop et al., 2014) suggesting that organic carbon burial was not the dominant control on CO_2 during that interval. Consequently, while carbon burial may occur prior to the OMT, other factors may act to keep atmospheric CO_2 levels at approximately constant levels.

The Mg/Ca-derived surface ocean temperatures at Site 926 show no clear temperature decrease during the OMT glaciation event (Figure 3), consistent with estimates of thermocline temperatures and planktic $\delta^{18}O$ estimates from the same site (Pearson et al., 1997; Stewart et al., 2017). Mg/Ca measured in thermocline dwelling *Dentoglobigerina venezuelana* at Site 926 shows no long-term change between 24.0 and 21.5 Ma, with temperature variations of less than 3°C across the interval, and no reduction in thermocline temperatures during the OMT glaciation (Stewart et al., 2017). In our new record, we see a counterintuitive multi-million year decrease in temperature of ~ 2°C between 24 and 22 Myrs and no clear relationship between temperature and $\delta^{18}O_{benthic}$. Temperatures decrease from ~ 28°C prior to the OMT, to values comparable to modern at 23 Ma (modern 26.7°C; Schlitzer, 2000). Several different factors could explain the lack of coherence between surface water temperature and the other proxy records such as (i) non-thermal control on Mg/Ca (e.g. salinity; e.g. Hönisch et al. 2013), (ii) variable degree of post-depositional dissolution of higher-Mg phases (Brown and Elderfield, 1996), or (iii) local influences on surface water temperature such as variability in the position of the ITCZ or changes in latitudinal heat transport (Hyeong et al., 2014). The inferred temperature offset between Site 926 and 872 may be real or attributed to the different taxa used between sites. Further work is needed at multiple sites in order to better understand the surface ocean temperature change associated with the OMT glaciation. We should stress, however, that the temperature effect on the calculation of CO_2 from $\delta^{11}B$ is relatively minor and we propagate a large uncertainty in SSTs (3°C; 2σ).

3.2 The relationship between $\delta^{11}B$ and $\delta^{18}O_{sw}$ across the transition at ODP Site 926

Benthic $\delta^{18}O$ is a compound record of local salinity, temperature and global continental ice volume changes. Salinity changes in the deep-sea are typically considered negligible and therefore if an independent reconstruction of temperature can be made the ice volume component ($\delta^{18}O_{sw}$) of the $\delta^{18}O$ record can be isolated. At ODP Site 926, a $\delta^{18}O_{sw}$ record was developed across the Oligocene-Miocene transition using Mg/Ca temperature estimates from *O. umbonatus* (Mawbey and Lear, 2013). To evaluate the relationship between $\delta^{18}O_{sw}$ and $\delta^{11}B$ across this interval we have interpolated the $\delta^{18}O_{sw}$ to our $\delta^{11}B$ age points and generated crossplots of the time equivalent data. The crossplots are based on changes in $\delta^{11}B$ and relative $\delta^{18}O_{sw}$, rather than CO_2 and ice volume, because the large uncertainties in $\delta^{11}B_{sw}$ and Mg/Ca_{sw} make it difficult to analyse the relationship between the two parameters. This treatment is appropriate because the seawater composition influences absolute values, but has a negligible effect on relative changes. That said, the uncertainty of the $\delta^{11}B$ and $\delta^{18}O_{sw}$ records is still relatively large, and there are relatively few data points defining each line, therefore these patterns should be treated as preliminary. While no relationship exists between ice volume and $\delta^{11}B/CO_2$ (R^2 = 0.06, p-value = 0.36) across the whole dataset, when the $\delta^{18}O_{sw}$ /$\delta^{11}B$ data points are split into peak glacial conditions (low sea level; Fig. 4 blue data points) and pre/post $\delta^{18}O$ excursion (Fig. 4; red data points) the data fall along two distinct trends. The exceptions to this finding are two $\delta^{11}B$ data points from within the OMT glaciation that coincide with the maximum in eccentricity when $\delta^{18}O_{sw}$ values were similar to pre/post OMT event conditions.

Based on the central estimates of the data available, the two different trend lines are statistically significant at the 95% confidence level and thus could reflect the different sensitivity of the ice sheet to CO_2 forcing under different orbital forcing. It is possible that the cool summers associated with low eccentricity would enable the ice sheet to expand further for a given CO_2 forcing compared to high eccentricity conditions, shifting these points from the other trend lines. Alternatively, the observed relationships could be interpreted as evidence for there being two components to the cryosphere, which respond differently for a given CO_2 forcing. Statistical analysis of a long Oligo-Miocene benthic $\delta^{18}O$ record from Walvis Ridge suggests that the OMT is characterised by more non-linear interactions compared to other intervals with similarly high amplitude $\delta^{18}O$ change, possibly related to cryosphere changes (Liebrand et al., 2017). While we cannot identify the ice sheet that forms during the OMT glaciation, the Greenland ice sheet, the marine-based West Antarctic ice sheet and sections of East Antarctic ice sheet have all been shown to be highly sensitive to CO_2 and orbital forcing (DeConto et al., 2008; Gasson et al., 2016b; Pollard and DeConto, 2009). While these new $\delta^{11}B$ data show some tentative evidence for both an orbital configuration and CO_2 control on ice sheet growth over the OMT, more data are clearly needed to further investigate these relationships.

3.3 ΔF_{CO2} associated with OMT deglaciation.

To assess the significance of CO_2 in driving the OMT deglaciation phase it is instructive to calculate the climate forcing change from the $\delta^{11}B$ data. The uncertainty in $\delta^{11}B_{sw}$ and the secondary carbonate system parameter become less significant when considering the relative change in CO_2 forcing on climate (ΔF_{CO2}) over short timescales (in this case over <1 million years), compared to when calculating absolute CO_2 (Hain et al. 2018). To further reduce uncertainty, we estimate the ΔF_{CO2} between two time windows, identified using the $\delta^{18}O_{benthic}$ records (Pälike et al., 2006a). A comparison is made between the peak glaciation (23.1-22.9 Ma) identified from the $\delta^{18}O_{benthic}$ record and a snapshot post event when $\delta^{18}O_{benthic}$ values have stabilised (22.7-22.2 Ma) following the post-OMT seafloor dissolution event (Mawbey and Lear, 2013). Based on this assessment we calculate that the rebound out of the OMT glaciation was associated with a change in radiative forcing of 1.15 W/m^2 (2σ range 0.8-1.5 W/m^2). However, we note that while comparing ΔF_{CO2} between two time windows reduces the calculated uncertainty, it may also underestimate the amplitude of ΔF_{CO2} as the CO_2 change associated with the maximum change in $\delta^{18}O_{sw}$ is not captured.

Our new ΔF_{CO2} estimate can then be compared to published estimates of $\Delta\delta^{18}O_{sw}$ to investigate the sensitivity of ice to CO_2-forcing over the OMT. Combining several estimates (Beddow et al., 2016; Mawbey and Lear, 2013; Mudelsee et al., 2014), the change in $\delta^{18}O_{sw}$ associated with the ΔF_{CO2} of ~1.15 W/m^2 can be estimated at -0.41 ±0.19 ‰ (Fig. 5). Intriguingly, this estimate is consistent with the range in $\Delta\delta^{18}O_{sw}$ modelled for a range of CO_2 change scenarios by Gasson et al. (2016b) (Fig. 5). In this way, our data support predictions from new-generation ice sheet models of a dynamic Antarctic ice sheet during the early Miocene that waxed and waned in response to both orbital configuration and atmospheric CO_2. However, we note that the changes in ice volume modelled by Gasson et al. (2016b) require extreme orbits in favour of Antarctic deglaciation, and it is as yet unclear what effect our observed CO_2 change would cause in these models under variable or average orbital configurations. Furthermore, the resolution of our data is not sufficient to determine whether the rate and timing of CO_2 and ice volume change is strictly comparable to that used in the modelling runs of Gasson et al., (2016b).

3.4 CO_2 changes prior to the OMT glaciation

While more robustly determined relative change in ΔF_{CO2} is clearly instructive, absolute reconstructions of CO_2 are required to shed light on the role of atmospheric CO_2 thresholds in the initiation of the OMT glaciation. Our new $\delta^{11}B$-CO_2 data suggest that CO_2 rises from a baseline value of ~265 ppm ($2\sigma\ ^{+166}_{-111}$ ppm), to ~325 ppm ($2\sigma\ ^{+218}_{-138}$ ppm) following the deglaciation (average CO_2 values are calculated from the post- and peak- glaciation windows defined in Figure 5). While the uncertainty on the CO_2 estimates is large, primarily as a result of large uncertainties on $\delta^{11}B_{sw}$ and DIC estimates (Supp. Fig 5), our data show that, within 1σ uncertainty (68% confidence interval; 200-345 ppm), CO_2 is below 400 ppm prior to, and during the Oligocene-Miocene transition (Fig. 3). Previous estimates of CO_2 across the OMT are sparse. Nonetheless, the absolute values of CO_2 reconstructed here agree well with the published alkenone records of Pagani et al., (2005) and Zhang et al., (2013) (when the data are plotted on the age model in Pagani et al., (2011) and updated to the Geological Timescale 2012 (Gradstein et al., 2012)), as well as leaf stomata CO_2 records of Kürschner et al., (2008) (Supp. Fig. 6). Based on the good agreement between alkenone and boron-isotope based CO_2 records across the OMT, in figure 6 we have plotted records derived using both methodologies to evaluate the multi-million year trends in CO_2 leading up to the OMT glaciation. The currently available data for the late Oligocene are sparse, however it appears that the OMT glaciation occurs following a multi-million year decrease in CO_2 and when the orbital forcing was favourable for ice growth. According to our combined multi-proxy dataset, the CO_2 decline begins at 29.5 Ma from values of ~1000 ppm to a minimum of ~265 ppm at 23.5 Ma (Fig 6).

A potential issue with the interpretation of a long-term late Oligocene CO_2 decrease is that the CO_2 fall between 27 and 24 Ma is at odds with the ~ 1‰ secular decrease in benthic $\delta^{18}O$ across the same interval, interpreted as an interval of climate warming and reduced ice volume (Mudelsee et al., 2014; Zachos et al., 2001a). One possibility is that climate – as far as it is represented by benthic $\delta^{18}O$ – and CO_2 were decoupled during the late Oligocene (as has been proposed for the Miocene; Herbert et al., 2016). A second possibility is that the relationship between Antarctic climate and deep-water temperature is not straightforward (Lear et al., 2015). For instance, a climate modelling study from the Mid-Miocene Climatic Transition suggests that the emplacement of an Antarctic ice sheet caused short-term Southern Ocean sea surface warming alongside deep-water cooling (Knorr and Lohmann, 2014). The hypothesised initiation or strengthening of the Antarctic circumpolar current (ACC) during the Late Oligocene (Hill et al., 2013; Ladant et al., 2014; Lyle et al., 2007; Pfuhl and McCave, 2005) may also have resulted in large oceanographic changes, with impacts on global temperatures and benthic foraminiferal $\delta^{18}O$, although the timing of ACC development is uncertain. A third possibility is that the ice volume accommodated on Antarctica was reduced during the Late Oligocene because of the tectonic subsidence of West Antarctica below sea level (Fretwell et al., 2013; Gasson et al., 2016b; Levy et al., 2016). Indeed, tectonic subsidence and a shift to smaller marine based ice sheets on West Antarctica during the Late Oligocene has been hypothesized to explain the long-term transition from highly symmetrical to saw-toothed $\delta^{18}O$ glacial-interglacial cycles (Liebrand et al., 2017). Finally, it is possible that the current estimates of CO_2 do not capture the full extent of the changes across this interval. More work is needed to better understand the relationship between ice volume and global climate changes of the Late Oligocene in order to give further context to the changes in CO_2, ice volume and climate across the OMT glaciation.

4. Conclusions

The new CO_2 data presented here, when combined with published Oligocene CO_2 data, suggests that the timing of the OMT glaciation is controlled by a combination of declining CO_2 below a critical threshold and a favorable orbital configuration for ice sheet expansion on Antarctica. This combination of factors has previously been used to explain the inception of sustained Antarctic glaciation across the Eocene-Oligocene transition, potentially pointing to a common behavior of the climate system as CO_2 levels approach an ice sheet expansion threshold through the Cenozoic. Our best estimate of CO_2 suggests that values were around ~265 ppm ($2\sigma\ ^{+166}_{-111}$ ppm) immediately prior to, and during the OMT glaciation and increased by ~65 ppm during the deglaciation phase. Further work is needed, however, to gain a deeper understanding of the background climate and CO_2 conditions during the late Oligocene so that the relative contribution of the different ice sheets to the ice volume changes associated with the OMT glaciation can be better determined.

Acknowledgements:

This work used samples provided by (I)ODP, which is sponsored by the US National Science Foundation, and participating countries under the management of Joint Oceanographic Institutions, Inc. We thank Walter Hale and Alex Wuelbers of the Bremen Core Repository for their kind assistance. The work was supported by NERC grants NE/I006176/1 (Gavin L. Foster and Caroline H. Lear), NE/I006427/1 (Caroline H. Lear), NE/K014137/1 and a Royal Society Wolfson Award (Paul A. Wilson), a NERC studentship (Rosanna Greenop) and financial support from the Welsh Government and Higher Education Funding Council for Wales through the Sêr Cymru National Research Network for Low Carbon, Energy and Environment (Sindia Sosdian). Diederik Liebrand and Richard Smith are thanked for helpful comments and discussion. Matthew Cooper, J. Andy Milton and the B-team are acknowledged for their assistance in the laboratory. All data are available as a supplement to this paper.

References:

Anand, P., Elderfield, H., and Conte, M. H. (2003), Calibration of Mg/Ca thermometry in planktonic foraminifera from a sediment trap time series, *Paleoceanography*, *18*(2), doi 10.1029/2002kpa000846

Bailey, I., Hole, G. M, Foster, G. L., Wilson, P. A., Storey, C. D., Trueman, C. N., and Raymo, M. E. (2013), An alternative suggestion for the Pliocene onset of major northern hemisphere glaciation based on the geochemical provenance of North Atlantic Ocean ice-rafted debris, *Quaternary Science Reviews*, *75*(0), 181-194.

Barker, S., Greaves, M., and Elderfield, H. (2003), A study of cleaning procedures used for foraminiferal Mg/Ca paleothermometry, *Geochemistry Geophysics Geosystems*, *4*(9), doi:10.1029/2003GC000559

Beddow, H. M., Liebrand, D., Sluijs, A., Wade, B. S., and Lourens, L. J. (2016), Global change across the Oligocene-Miocene transition: High-resolution stable isotope records from IODP Site U1334 (equatorial Pacific Ocean), *Paleoceanography*, *31*(1), 81-97.

Brennan, S. T., Lowenstein, T. K., and Cendón, D. I., (2013), The major-ion composition of Cenozoic seawater: The past 36 million years from fluid inclusions in marine halite, *American Journal of Science*, *313*(8), 713-775.

Brown, S. J., and H. Elderfield (1996), Variations in Mg/Ca and Sr/Ca ratios of planktonic foraminifera caused by postdepositional dissolution: Evidence of shallow Mg-dependent dissolution, *Paleoceanography*, 11(5), 543–551, doi: 10.1029/96PA01491.

Byrne, B., and Goldblatt, C. (2014), Radiative forcing at high concentrations of well-mixed greenhouse gases, *Geophysical Research Letters*, *41*(1), 152-160.

Catanzaro, E. J., Champion, C., Garner, E., Marinenko, G., Sappenfield, K., and Shields, S. W. (1970), *Boric Acid: Isotopic and Assay Standard Reference Materials NBS (US) Special Publications. National Bureau of Standards, Institute for Materials Research*, Washington, DC.

Coxall, H. K., Wilson, P. A., Palike, H., Lear, C. H., and Backman, J. (2005), Rapid stepwise onset of Antarctic glaciation and deeper calcite compensation in the Pacific Ocean, *Nature*, *433*(7021), 53-57.

DeConto, R. M., and Pollard, D. (2003), A coupled climate-ice sheet modeling approach to the Early Cenozoic history of the Antarctic ice sheet, *Palaeogeography Palaeoclimatology Palaeoecology*, *198*(1-2), 39-52.

DeConto, R. M., Pollard, D., Wilson, P. A., Palike, H., Lear, C. H., and Pagani, M. (2008), Thresholds for Cenozoic bipolar glaciation, *Nature*, *455*(7213), 652-656.

Delany, M. L., Be, A. W. H., and Boyle E. A. (1985), Li, Sr, Mg and Na in foraminiferal calcite shells from laboratory culture, sediment traps, and sediment cores, *Geochimica Et Cosmochimica Acta*, *49*(6), 1327-1341.

Edgar, K. M., Wilson, P. A., Sexton, P. F., and Suganuma, Y. (2007), No extreme bipolar glaciation during the main Eocene calcite compensation shift, *Nature*, *448*(7156), 908-911.

Eldrett, J. S., Harding, I. C, Wilson, P. A., Butler, E., and Roberts, A. P. (2007), Continental ice in Greenland during the Eocene and Oligocene, *Nature*, *446*, 176-179.

Evans, D., and Muller, W. (2012), Deep time foraminifera Mg/Ca paleothermometry: Nonlinear correction for secular change in seawater Mg/Ca, *Paleoceanography*, *27*, PA4205, doi:10.1029/2012PA002315

Foster, G., Lear, C. H., and Rae, J. W. B. (2012), The evolution of pCO_2, ice volume and climate during the middle Miocene, *Earth and Planetary Science Letters*, *341-344*, 243-254.

Foster, G. L. (2008), Seawater pH, pCO_2 and $[CO_3^{2-}]$ variations in the Caribbean Sea over the last 130 kyr: A boron isotope and B/Ca study of planktic forminifera, *Earth and Planetary Science Letters*, *271*(1-4), 254-266.

Foster, G. L., and Rohling, E. J. (2013), Relationship between sea level and climate forcing by CO_2 on geological timescales, *Proceedings of the National Academy of Sciences of the United States of America*, *110*(4), 1209-1214.

Foster, G. L., Lunt, D. J., and Parrish, R. R. (2010), Mountain uplift and the glaciation of North America – a sensitivity study, *Clim. Past*, *6*(5), 707-717.

Foster, G. L., Hönisch, B., Paris, G., Dwyer, G. S., Rae, J. W. B, Elliott, T., Gaillardet, J., Hemming, N.G., Louvat, P., and Vengosh, A. (2013), Interlaboratory comparison of boron isotope analyses of boric acid, seawater and marine $CaCO_3$ by MC-ICPMS and NTIMS, *Chemical Geology*, *358*, 1-14.

Fretwell, P., et al. (2013), Bedmap2: improved ice bed, surface and thickness datasets for Antarctica, *The Cryosphere*, *7*(1), 375-393.

Gasson, E., DeConto, R. M., and Pollard D. (2016a), Modeling the oxygen isotope composition of the Antarctic ice sheet and its significance to Pliocene sea level, *Geology*, *44*(10), 827-830.

Gasson, E., DeConto, R. M., Pollard, D., and Levy, R. H. (2016b), Dynamic Antarctic ice sheet during the early to mid-Miocene, *Proceedings of the National Academy of Sciences*, *113*(13), 3459-3464.

Gasson, E., Siddall, M., Lunt, D. J, Rackham, O.. J. L., Lear, C. H., and Pollard, D. (2012), Exploring Uncertainties in the Relationship between Temperature, Ice Volume, and Sea Level over the Past 50 Million Years, *Rev Geophys*, *50*, RG1005, doi:10.1029/2011RG000358

Gradstein, F. M., Ogg, J. G. and Schmitz, M. (2012), *The Geologic Time Scale 2012*, Elsevier, Amsterdam.

Greenop, R., Foster, G. L., Wilson, P. A., and Lear, C. H. (2014), Middle Miocene climate instability associated with high-amplitude CO_2 variability, *Paleoceanography*, *29*(9), doi: 10.1002/2014PA002653

Greenop, R., Hain, M.P., Sosdian, S. M., Oliver, K. I. C., Goodwin, P., Chalk, T. B., Lear, C. H., Wilson, P. A., and Foster, G. L. (2017), A record of Neogene seawater $\delta^{11}B$ reconstructed from paired $\delta^{11}B$ analyses on benthic and planktic foraminifera, *Clim. Past*, *13*(2), 149-170.

Hain, M. P., Sigman, D. M., Higgins, J. A., and Haug, G. H. (2015), The effects of secular calcium and magnesium concentration changes on the thermodynamics of seawater acid/base chemistry: Implications for Eocene and Cretaceous ocean carbon chemistry and buffering, *Global Biogeochem Cy*, *29*(5), 517-533.

Hain, M. P., Foster, G. L., and Chalk, T. B. (2018), Robust Constraints on Past CO_2 Climate Forcing From the Boron Isotope Proxy, *Paleoceanography and Paleoceanoclimatology*, *33*(10), 1099-1115, https://doi.org/10.1029/2018PA003362.

Hasiuk, F., and Lohmann, K. (2010), Application of calcite Mg partitioning functions to the reconstruction of paleocean Mg/Ca, *Geochimica Et Cosmochimica Acta*, *74*(23), 6751-6763.

Haug, G. H., and Tiedemann, R. (1998), Effect of the formation of the Isthmus of Panama on Atlantic Ocean thermohaline circulation, *Nature*, *393*(6686), 673-676.

Henehan, M. J., Foster, G. L., Bostock, H. C., Greenop, R., Marshall, B. J., and Wilson, P. A. (2016), A new boron isotope-pH calibration for Orbulina universa, with implications for understanding and accounting for 'vital effects', *Earth and Planetary Science Letters*, *454*, 282-292.

Henehan, M. J., et al. (2013), Calibration of the boron isotope proxy in the planktonic foraminifera Globigerinoides ruber for use in palaeo-CO_2 reconstruction, *Earth and Planetary Science Letters*, *364*(0), 111-122.

Herbert, T. D., Lawrence, K. T., Tzanova, A., Peterson, L. C., Caballero-Gill, R., and Kelly, C.S. (2016), Late Miocene global cooling and the rise of modern ecosystems, *Nature Geoscience*, *9*, 843-847.

Hill, D., Haywood, A., Valdes, P., Francis, J., Lunt, D., Wade, B., and Bowman, V. (2013), Paleogeographic controls on the onset of the Antarctic circumpolar current, *Geophysical Research Letters*, *40*(19), 5199-5204.

Hönisch, B., Bijma, J., Russell, A. D., Spero, H. J., Palmer, M. R., Zeebe, R. E., and Eisenhauer, A. (2003), The influence of symbiont photosynthesis on the boron isotopic composition of foraminifera shells, *Marine Micropaleontology*, *49*(1-2), 87-96.

Hönisch, B., Allen, K. A., Lea, D. W., Spero, H. J., Eggin, S. M., Arbuszewski, J., deMenocal, P., Rosenthal, Y., Russell, A.D., and Elderfield, H. (2013), The influence of salinity on Mg/Ca in planktic foraminifers—Evidence from cultures, core-top sediments and complementary $\delta^{18}O$, *Geochim. Cosmochim. Acta*, *121*, 196–213.

Horita, J., Zimmermann, H., and Holland, H. D., (2002), Chemical evolution of seawater during the Phanerozoic: Implications from the record of marine evaporites, *Geochimica Et Cosmochimica Acta*, *66*(21), 3733-3756.

Hyeong, K., Lee, J., Seo, I., Lee, M. J., Yoo, C. M., and Khim. B-K. (2014), Southward shift of the Intertropical Convergence Zone due to Northern Hemisphere cooling at the Oligocene-Miocene boundary, *Geology*, *42*(8): 667–670. doi: https://doi.org/10.1130/G35664.1

Klochko, K., Kaufman, A. J., Yao, W.S., Byrne, R. H., and Tossell, J. A. (2006), Experimental measurement of boron isotope fractionation in seawater, *Earth and Planetary Science Letters*, *248*(1-2), 276-285.

Knorr, G., and Lohmann, G. (2014), Climate warming during Antarctic ice sheet expansion at the Middle Miocene transition, *Nature Geosci*, *7*(5), 376-381.

Kürschner, W. M., Kvaček, Z., and Dilcher, D.L. (2008), The impact of Miocene atmospheric carbon dioxide fluctuations on climate and the evolution of terrestrial ecosystems, *Proceedings of the National Academy of Sciences of the United States of America*, *105*(2), 449-453.

Ladant, J. B., Donnadieu, Y., and Dumas, C. (2014), Links between CO_2, glaciation and water flow: reconciling the Cenozoic history of the Antarctic Circumpolar Current, *Clim. Past*, *10*(6), 1957-1966.

Langebroek, P. M., Paul, A., and Schulz, M. (2010), Simulating the sea level imprint on marine oxygen isotope records during the middle Miocene using an ice sheet-climate model, *Paleoceanography*, *25*, PA4203, doi:10.1029/2008PA001704

Laskar, J., Robutel, P., Joutel, F., Gastineau, M., Correia, A. C. M., and Levrard, B. (2004), A long-term numerical solution for the insolation quantities of the Earth, *Astron Astrophys*, *428*(1), 261-285.

Lear, C. H., Rosenthal, Y., Coxall, H. K., and Wilson, P.A. (2004), Late Eocene to early Miocene ice sheet dynamics and the global carbon cycle, *Paleoceanography*, *19*(4), PA4015, doi:10.1029/2004PA001039

Lear, C. H., Coxall, H. K., Foster, G. L., Lunt, D. J., Mawbey, E. M., Rosenthal, Y., Sosdian, S. M., Thomas, E., and Wilson, P.A. (2015), Neogene ice volume and ocean temperatures: Insights from infaunal foraminiferal Mg/Ca paleothermometry, *Paleoceanography*, *30*(11), 1437-1454.

Lemarchand, D., Gaillardet, J., Lewin, E., and Allegre, C.J . (2000), The influence of rivers on marine boron isotopes and implications for reconstructing past ocean pH, *Nature*, *408*(6815), 951-954.

Levy, R., et al. (2016), Antarctic ice sheet sensitivity to atmospheric CO_2 variations in the early to mid-Miocene, *Proceedings of the National Academy of Sciences*, *113*(13), 3453-3458.

Liebrand, D., Lourens, L. J., Hodell, D. A., de Boer, B., van de Wal, R. S. W., and Palike, H. (2011), Antarctic ice sheet and oceanographic response to eccentricity forcing during the early Miocene, *Climate of the Past*, *7*(3), 869-880.

Liebrand, D., et al. (2017), Evolution of the early Antarctic ice ages, *Proceedings of the National Academy of Sciences*, *114*(15), 3867-3872.

Lüthi, D., et al. (2008), High-resolution carbon dioxide concentration record 650,000-800,000 years before present, *Nature*, *453*(7193), 379-382.

Lyle, M., Gibbs, S., Moore, T., and Rea, D. (2007), Late Oligocene initiation of the Antarctic circumpolar current: Evidence from the South Pacific, *Geology*, *35*(8), 691-694.

Martínez-Botí, M. A., Marino, G., Foster, G. L., Ziveri, P., Henehan, M. J., Rae, J. W. B., Mortyn, P. G., and Vance, D. (2015), Boron isotope evidence for oceanic carbon dioxide leakage during the last deglaciation, *Nature*, *518*(7538), 219-222.

Martínez-Botí, M. A., Foster, G. L., Chalk, T. B., Rohling, E. J., Sexton, P. F., Lunt, D. J., Pancost, R. D., Badger, M. P. S, and Schmidt D. N. (2015), Plio-Pleistocene climate sensitivity evaluated using high-resolution CO_2 records, *Nature*, *518*, 49.

Mawbey, E. M., and Lear, C. H. (2013), Carbon cycle feedbacks during the Oligocene-Miocene transient glaciation, *Geology*, *41*(9), 963-966.

Miller, K. G., Wright, J. D., and Fairbanks, R. G., (1991), Unlocking the Ice House - Oligocene-Miocene Oxygen Isotopes, Eustasy, and Margin Erosion, *Journal of Geophysical Research-Solid Earth and Planets*, *96*(B4), 6829-6848.

Mudelsee, M., Bickert, T., Lear, C. H., and Lohmann, C. (2014), Cenozoic climate changes: A review based on time series analysis of marine benthic $\delta^{18}O$ records, *Reviews of Geophysics*, *52*(3), 333-374.

Naish, T. R., et al. (2001), Orbitally induced oscillations in the East Antarctic ice sheet at the Oligocene/Miocene boundary, *Nature*, *413*(6857), 719-723.

Pagani, M., Zachos, J. C., Freeman, K. H., Tipple, B., and Bohaty, S. (2005), Marked decline in atmospheric carbon dioxide concentrations during the Paleogene, *Science*, *309*(5734), 600-603.

Pagani, M., Huber, M., Liu, Z., Bohaty, S., Henderiks, J., Sijp, W., Krishnan, S., and DeConto, R. (2011), The Role of Carbon Dioxide During the Onset of Antarctic Glaciation, *Science*, *334*(6060), 1261-1264.

Pälike, H., Frazier, J., and Zachos, J. C. (2006a), Extended orbitally forced palaeoclimatic records from the equatorial Atlantic Ceara Rise, *Quaternary Science Reviews*, *25*(23-24), 3138-3149.

Pälike, H., Norris, R. D., Herrle, J. O., Wilson, P. A., Coxall, H. K., Lear, C. H., Shackleton, N. J., Tripati, A. K., and Wade, B. S. (2006b), The Heartbeat of the Oligocene Climate System, *Science*, *314*(5807), 1894-1898.

Palmer, M. R., Pearson, P. N., and Cobb, S. J. (1998), Reconstructing past ocean pH-depth profiles, *Science*, *282*(5393), 1468-1471.

Paul, H., Zachos, J. C., Flower, B., and Tripati, A. (2000), Orbitally induced climate and geochemical variability across the Oligocene/Miocene boundary, *Paleoceanography*, 471-485.

Pearson, P. N., Shackleton, N. J., Weedon, G. P., & Hall, M. A. (1997). Multispecies planktonic foraminifera stable isotope stratigraphy through Oligocene/Miocene boundary climatic cycles, site 926. In N. J. Shackleton, et al. (Eds.), Proceedings of the Ocean Drilling Program, Scientific Results (Vol. 154, pp. 441‑449). College Station, TX: Ocean Drilling Program

Pearson, P. N., and Palmer, M. R. (2000), Atmospheric carbon dioxide concentrations over the past 60 million years, *Nature*, *406*(6797), 695-699.

Pearson, P. N., and Wade, B. S. (2009), Taxonomy and Stable Isotope Paleoecology of Well-Preserved Planktonic Foraminifera from the Uppermost Oligocene of Trinidad, *Journal of Foraminiferal Research*, *39*(3), 191-217.

Pearson, P. N., Foster, G. L., and Wade, B. S. (2009), Atmospheric carbon dioxide through the Eocene-Oligocene climate transition, *Nature*, *461*(7267), 1110-1113.

Pekar, S. F., Christie-Blick, N., Kominz, M. A., and Miller, K. G. (2002), Calibration between eustatic estimates from backstripping and oxygen isotopic records for the Oligocene, *Geology*, *30*(10), 903-906.

Pfuhl, H., and McCave, I. (2005), Evidence for late Oligocene establishment of the Antarctic Circumpolar Current, *Earth and Planetary Science Letters*, *235*(3-4), 715-728.

Pollard, D., and DeConto, R. M. (2005), Hysteresis in Cenozoic Antarctic ice-sheet variations, *Global and Planetary Change*, *45*(1-3), 9-21.

Pollard, D., and DeConto, R. M. (2009), Modelling West Antarctic ice sheet growth and collapse through the past five million years, *Nature*, *458*(7236), 329-332.

Pollard, D., DeConto, R. M., and Alley, R. B. (2015), Potential Antarctic Ice Sheet retreat driven by hydrofracturing and ice cliff failure, *Earth and Planetary Science Letters*, *412*, 112-121.

Raitzsch, M., and Hönisch, B. (2013), Cenozoic boron isotope variations in benthic foraminifers, *Geology*, *41*(5), 591-594.

Sanyal, A., Bijma, J., Spero, H., and Lea, D. W. (2001), Empirical relationship between pH and the boron isotopic composition of Globigerinoides sacculifer: Implications for the boron isotope paleo-pH proxy, *Paleoceanography*, *16*(5), 515-519.

Schlitzer, R., (2000) Electronic Atlas of WOCE Hydrographic and Tracer Data Now Available, *Eos Trans. AGU*, *81*(5), 45.

Schlitzer, R. (2017), Ocean Data View, *odv.awi.de*.

Seki, O., Foster, G. L., Schmidt, D. N., Mackensen, A., Kawamura, K., and Pancost, R.D. (2010), Alkenone and boron-based Pliocene pCO_2 records, *Earth and Planetary Science Letters*, *292*(1-2), 201-211.

Sosdian, S., Greenop, R., Hain, M. P., Foster, H. L., Pearson, P. N., and Lear, C. H. (2018), Constraining the evolution of Neogene ocean carbonate chemistry using the boron isotope pH proxy, *Earth and Planetary Science Letters*. *498*, 362-376.

Stewart, J. A., James, R. H., Anand, P., & Wilson, P. A. (2017). Silicate weathering and carbon cycle controls on the Oligocene-Miocene transition glaciation. *Paleoceanography*, 32. https://doi. org/10.1002/2017PA003115

Takahashi, T., et al. (2009), Climatological mean and decadal change in surface ocean pCO_2, and net sea-air CO_2 flux over the global oceans, *Deep-Sea Res Pt I*, *56*(11), 2075-2076.

Zachos, J., Pagani, M., Sloan, L., Thomas, E., and Billups, K. (2001a), Trends, rhythms, and aberrations in global climate 65 Ma to present, *Science*, 686-693.

Zachos, J., Shackleton, N., Revenaugh, J., Palike, H., and Flower, B. P. (2001b), Climate response to orbital forcing across the Oligocene-Miocene boundary, *Science*, 274-278.

Zachos, J. C., Flower, B. P. and Paul, H. (1997), Orbitally paced climate oscillations across the Oligocene/Miocene boundary, *Nature*, *388*(6642), 567-570.

Zachos, J. C., Dickens, G. R., and Zeebe, R. E. (2008), An early Cenozoic perspective on greenhouse warming and carbon-cycle dynamics, *Nature*, *451*(7176), 279-283.

Zeebe, R. E., Wolf-Gladrow, D. A., Bijma, J., and Hönisch, B. (2003), Vital effects in foraminifera do not compromise the use of $\delta^{11}B$ as a paleo-pH indicator: Evidence from modeling, *Paleoceanography*, *18*(2), 1043, doi:10.1029/2003PA000881

Zhang, Y. G., Pagani, M., Liu, Z. H., Bohaty, S., and DeConto, R. (2013), A 40-million-year history of atmospheric CO_2, *Philosophical Transactions of the Royal Society A: Mathematical, Physical and Engineering Sciences*, *371*(2001), http://dx.doi.org/10.1098/rsta.2013.0096

Figures Captions

Figure 1: Climate and forcing over the Oligocene-Miocene transition. a) Cenozoic oxygen isotope composite (Zachos et al., 2008) (b) Oxygen isotope records from Site 926 (light blue) (Pälike et al., 2006a), Site U1334 (dark blue) (Beddow et al., 2016), Site 1264 (light green) (Liebrand et al., 2011) and Site 1218 (dark green) (Pälike et al., 2006b and references therein). (c) Eccentricity orbital forcing from Laskar et al., (2004). (d) Carbon isotope records from Site 926 (light blue) (Pälike et al., 2006a), Site U1334 (dark blue) (Beddow et al., 2016), Site 1264 (light green) (Liebrand et al., 2011) and Site 1218 (dark green) (Pälike et al., 2006b and references therein). (e) Obliquity orbital forcing from Laskar et al., (2004). (f) Previously published CO_2 records from across the OMT glaciation. Alkenone reconstructions (light blue and purple) from Pagani et al., (2005) and (dark blue) from Zhang et al., (2013) plotted on the age model of Pagani et al., (2011) updated to Gradstein et al., (2012). Leaf stomata CO_2 reconstruction (yellow diamond) from Kürschner et al., (2008). The Oligocene-Miocene transition is highlighted in red.

Figure 2: Map of study sites and mean annual air-sea disequilibria with respect to pCO_2. The black dots indicate the location of the sites used in this study. ODP Site 926 (3°43.148′N, 42°54.507′W) is at a water depth of 3598 m and the modern extent of disequilibria is ~ +22 ppm. ODP Site 872C (10°05.62’N, 162°52.002’E) is at a water depth of 1082 m and the modern extent of disequilibria is ~ 0 ppm. Data are from Takahashi et al., (2009). Plotted using ODV (Schlitzer, 2017).

Figure 3: New Oligocene-Miocene SST/CO_2 estimates and published climate records. (a) $\delta^{18}O$ record from Site 926 (Pälike et al., 2006a and references therein). (b)

Oligocene-Miocene transition $\delta^{11}B$ from Site 926 (red) and Site 872 (blue) from this study and Greenop et al., (2017). The data are plotted on inverted axes and the error bars show the external reproducibility at 95% confidence. (c) Oligocene-Miocene transition Mg/Ca temperature estimates from Site 926 (red) and Site 872 (blue) from this study and Greenop et al., (2017). Temperature is calculated using the generic Mg/Ca temperature calibration of Anand et al., (2003). 3°C error bar reflects the 2σ temperature uncertainty that was propagated through the CO_2 calculation. (d) Eccentricity orbital forcing from Laskar et al., (2004). (e) Oligocene-Miocene transition CO_2 from Site 926 (red) and Site 872 (blue) calculated from $\delta^{11}B$ data from this study and Greenop et al., (2017). Dark and light bands show CO_2 uncertainty at the 68% confidence interval and the 95% confidence interval respectively at Site 926 (red) and Site 872 (blue). Uncertainty was calculated using a Monte Carlo simulation (n=30000) including uncertainty in temperature, salinity, the DIC relationship, $\delta^{11}B_{sw}$ and the $\delta^{11}B$ measurement. See text for details of the measurement and uncertainty. (f) Obliquity orbital forcing from Laskar et al. (2004). Orange shaded area highlights the Oligocene-Miocene transition.

Figure 4: The relationship between $\delta^{11}B$ and $\delta^{18}O_{sw}$. (a) The $\delta^{11}B$ record from Site 926 focused on 22.7-23.4 Ma from this study and Greenop et al., (2017). The pink circles highlight $\delta^{11}B$ samples that fall within 'peak glaciation conditions' but show a better fit on the pre/post OMT glaciation event line (see text for details). Note the axis is reversed. (b) Relative $\delta^{18}O_{sw}$ change color-coded for peak glacial (blue) and pre/post glacial conditions (red) (Mawbey and Lear, 2013). Open circles are $\delta^{18}O_{sw}$ estimates within the 'dissolution event' and therefore bias towards negative values. The dashed black lines show the coincident timing of the two $\delta^{11}B$ data points that sit on the pre-/post- OMT glaciation event line and the eccentricity paced high sea level events within the OMT glaciation. Note the inverted axis. (c) Time equivalent crossplot of $\delta^{11}B$ (error bars external reproducibility at 95% confidence) and relative $\delta^{18}O_{sw}$ (error bars ±0.2‰). The peak glacial (blue) and pre/post OMT glaciation (red) data plot along two separate lines. Dotted lines are the 95% confidence intervals on the fit of the linear regressions. The pink data points fall within the glacial interval (circled in panel (a)) but plot on the pre/post glacial line (see text for details).

Figure 5: Oligocene-Miocene transition relative climate forcing. (a) $\delta^{18}O$ record from Site 926 (Pälike et al., 2006a and references therein). (b) Relative climate forcing across the OMT calculated from $\delta^{11}B$ data from this study and Greenop et al., (2017) (see text for details). Dark and light bands show the uncertainty on relative climate forcing at the 68% confidence interval and the 95% confidence interval respectively at Site 926 (red) and Site 872 (blue). All climate forcing is calculated relative to the data point at 24.02 Ma. The dashed box and purple shaded area highlights the two windows relative climate forcing is calculated from for the data in panel (c). In order to investigate the step-change in CO_2 associated with the deglaciation we have excluded any data within the deep-ocean dissolution event (Mawbey and Lear 2013) between 22.9 and 22.8 Ma where $\delta^{11}B$ is highly variable. (c) Relative climate forcing (with 95% confidence interval; red box) for data from this study plotted with an estimate of OMT relative $\delta^{18}O_{sw}$ change (-0.41 ±0.19‰) (see text for details). The modelled CO_2 from Gasson et al., (2016a) converted to relative climate forcing is also plotted with the model output $\delta^{18}O_{sw}$ and shows good agreement with our data (orange circles).

Figure 6: Long-term Oligocene climate and CO_2. (a) $\delta^{18}O$ record from Site 1218 (Pälike et al., 2006b and references therein). (b) Obliquity orbital forcing from Laskar et al., (2004) (c) $\delta^{11}B$-CO_2 from Site 926 (calculated from $\delta^{11}B$ data from this study and Greenop et al., (2017)) in red and Site 872 (this study) in dark blue, alkenone-derived CO_2 from Zhang et al., (2013) in light blue and $\delta^{11}B$-CO_2 from Pearson et al., (2009) in orange. For $\delta^{11}B$-derived CO_2 records error bars represent 2σ uncertainty.

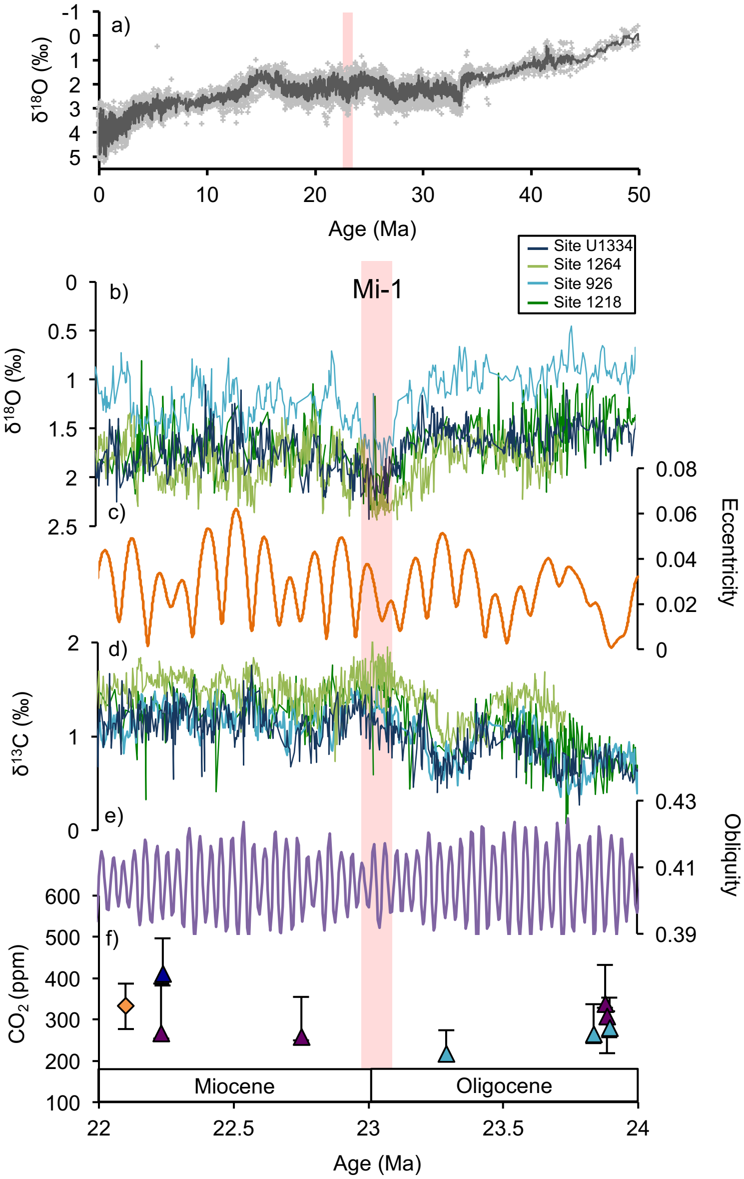
a)
δ18O (‰)
-1
0
1
2
3
4
5
0
10
20
30
40
50
Age (Ma)
Site U1334
Site 1264
Site 926
Site 1218
b)
Mi-1
δ18O (‰)
0
0.5
1
1.5
2
2.5
c)
0.08
0.06
0.04
0.02
0
Eccentricity
d)
δ13C (‰)
2
1
0
e)
0.43
0.41
0.39
Obliquity
f)
CO2 (ppm)
600
500
400
300
200
100
Miocene
Oligocene
22
22.5
23
23.5
24
Age (Ma)

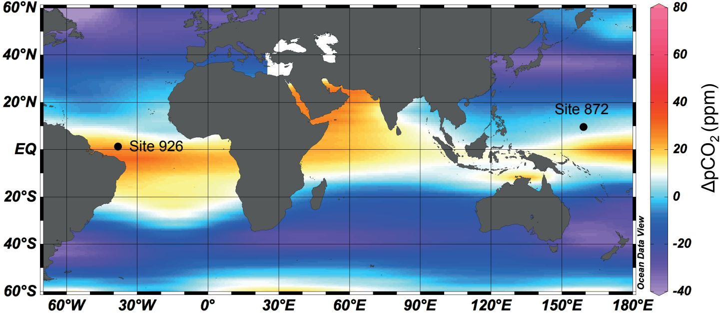

60°N
40°N
20°N
EQ
20°S
40°S
60°S
60°W
30°W
0°
30°E
60°E
90°E
120°E
150°E
180°E
Site 926
Site 872
Ocean Data View
80
60
40
20
0
-20
-40
ΔpCO_2 (ppm)

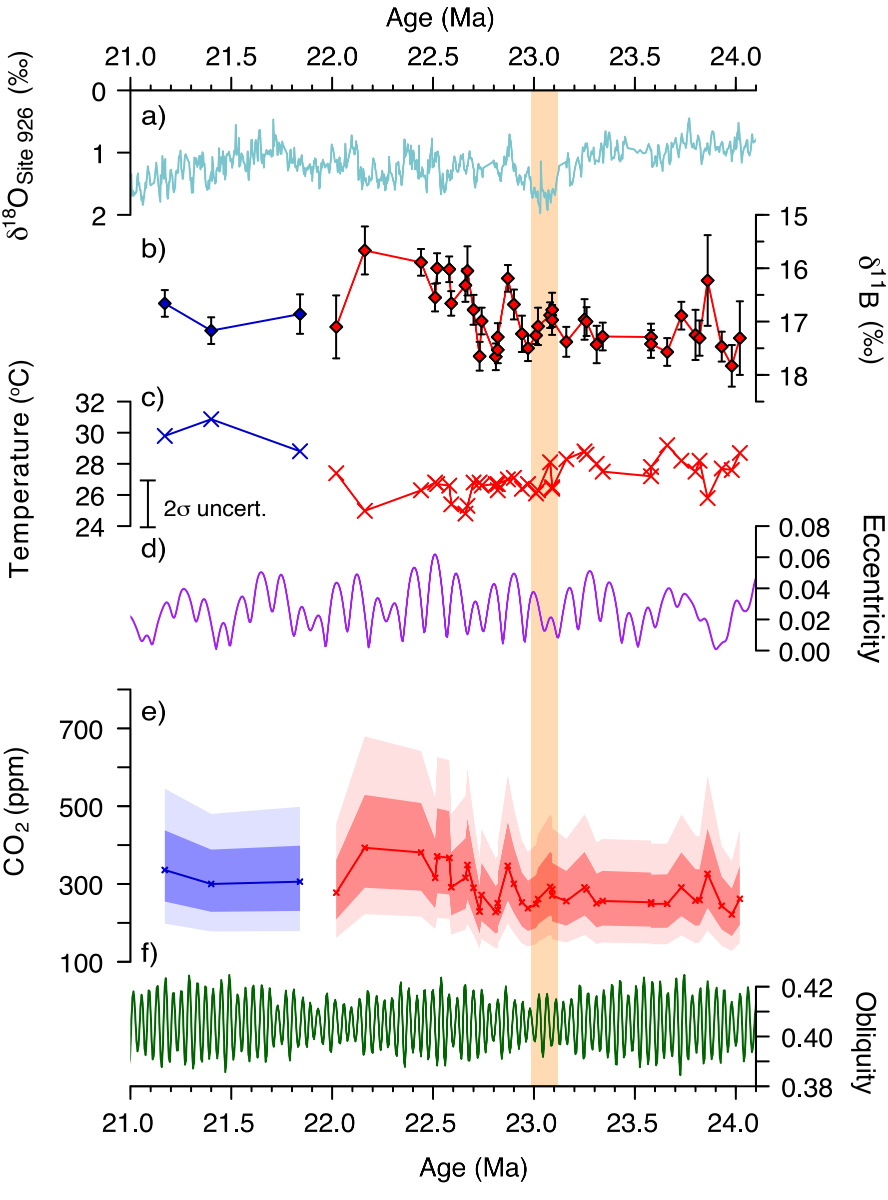

Age (Ma)
21.0
21.5
22.0
22.5
23.0
23.5
24.0
$\delta^{18}O_{Site\ 926}$ (‰)
0
1
2
a)
b)
$\delta^{11}B$ (‰)
15
16
17
18
c)
Temperature (°C)
32
30
28
26
24
2σ uncert.
d)
Eccentricity
0.08
0.06
0.04
0.02
0.00
e)
CO_2 (ppm)
700
500
300
100
f)
Obliquity
0.42
0.40
0.38
21.0
21.5
22.0
22.5
23.0
23.5
24.0
Age (Ma)

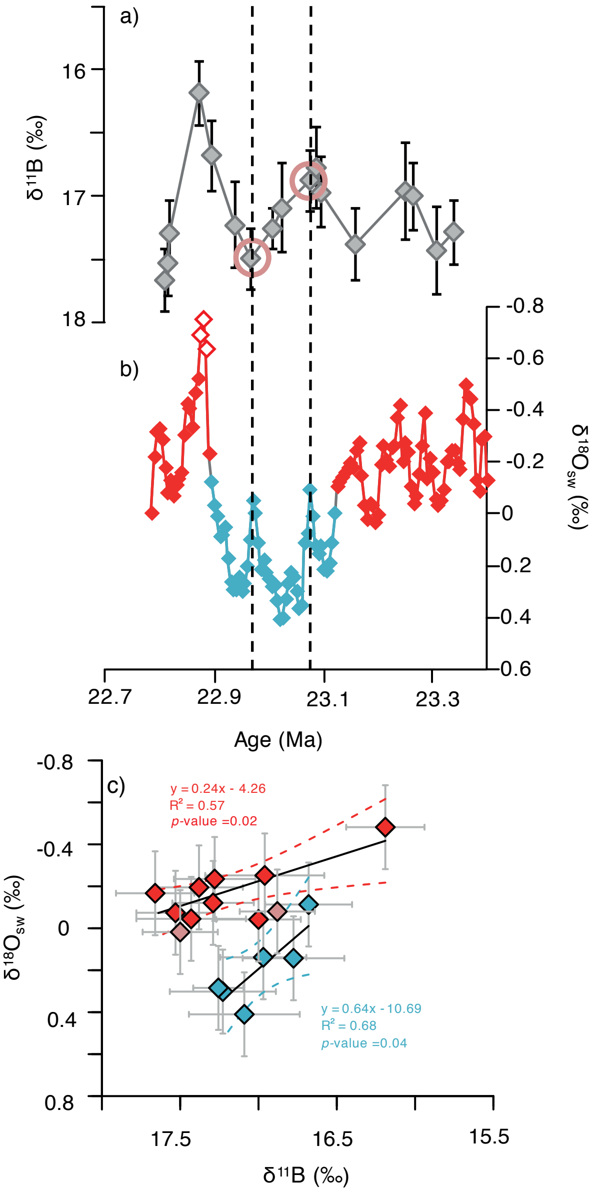

a)
16
17
18
δ11B (‰)
b)
-0.8
-0.6
-0.4
-0.2
0
0.2
0.4
0.6
δ18Osw (‰)
22.7
22.9
23.1
23.3
Age (Ma)
c)
-0.8
-0.4
0
0.4
0.8
δ18Osw (‰)
y = 0.24x - 4.26
R2 = 0.57
p-value =0.02
y = 0.64x - 10.69
R2 = 0.68
p-value =0.04
17.5
16.5
15.5
δ11B (‰)

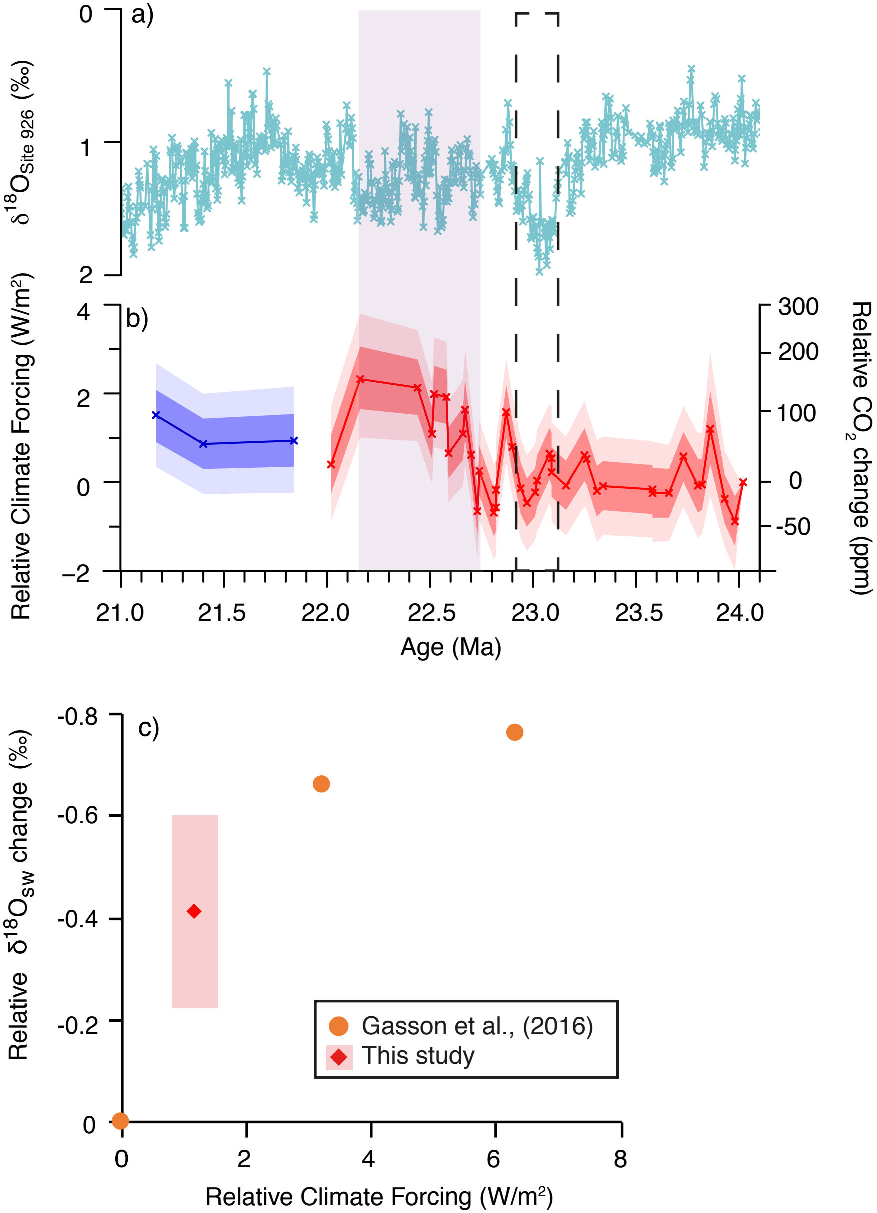

a)
b)
c)
$\delta^{18}O_{Site\ 926}$ (‰)
0
1
2
Relative Climate Forcing (W/m²)
4
2
0
−2
300
200
100
0
-50
Relative CO_2 change (ppm)
21.0
21.5
22.0
22.5
23.0
23.5
24.0
Age (Ma)
Relative $\delta^{18}O_{sw}$ change (‰)
-0.8
-0.6
-0.4
-0.2
0
0
2
4
6
8
Relative Climate Forcing (W/m²)
Gasson et al., (2016)
This study

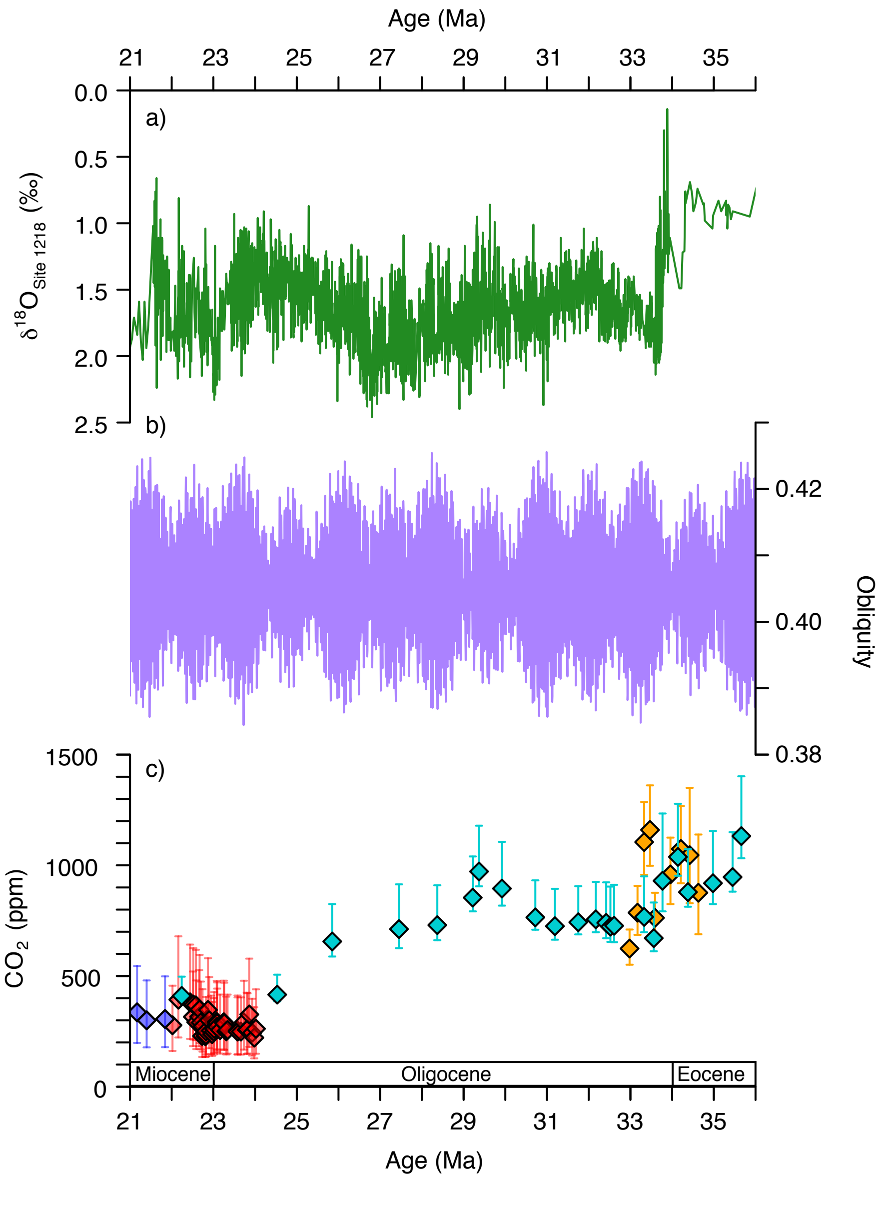

Age (Ma)
21
23
25
27
29
31
33
35
0.0
0.5
1.0
1.5
2.0
2.5
a)
$\delta^{18}O_{Site\ 1218}$ (‰)
b)
0.42
0.40
0.38
Obliquity
c)
1500
1000
500
0
CO_2 (ppm)
Miocene
Oligocene
Eocene
Age (Ma)

Paleoceanography and Paleoclimatology

Supporting Information for

Orbital forcing, ice-volume and CO_2 across the Oligocene-Miocene Transition

Rosanna Greenop[1, 2], Sindia M. Sosdian[3], Michael J. Henehan[4], Paul A. Wilson[1], Caroline H. Lear[3] and Gavin L. Foster[1]

[1] School of Ocean and Earth Science, National Oceanography Centre Southampton, University of Southampton Waterfront Campus, European Way, Southampton, SO14 3ZH, UK.

[2] School of Earth and Environmental Science, Irvine Building, University of St Andrews, North Street, St Andrews, KY16 9AL, UK.

[3] School of Earth and Ocean Sciences, Cardiff University, Main Building, Park Place, Cardiff, CF10 3AT.

[4] GFZ German Research Centre for Geosciences, Telegrafenberg, 14473, Potsdam, Germany

Contents of this file

Figures S1 to S6

Additional Supporting Information (Files uploaded separately)

Caption for Datasets S1

Introduction

This supporting information file contains 6 supplementary figures showing boron isotope calibration lines at three different $\delta^{11}B_{sw}$ values (Fig S1), the translated modern calibrations for different values of past $\delta^{11}B_{sw}$ (Fig S2), the input parameters into the $\delta^{11}B$-pH calculations (Fig S3), CO_2 calculated using the logDIC regression estimated using three different $\delta^{11}B_{sw}$ records (Fig S4), the sensitivity of pH and CO_2 to estimated $\delta^{11}B_{sw}$ and DIC (Fig S5) and a comparison of new and published OMT CO_2 estimates (Fig S6).

Dataset S1 contains new and published $\delta^{11}B$ and Mg/Ca data from ODP Site 926 and ODP Site 872 (from Greenop et al., 2017 and this study) with estimates of CO_2/SST (from this study) and

$\delta^{18}O_{sw}$ (from Mawbey and Lear, 2013). For details of the SST/CO_2 calculations see main text. Age models for Site 926 and Site 872 are from Pälike et al., (2006a) (and references therein) and Sosdian et al., (2018) updated to GTS2012 (Gradstein et al., 2012) respectively.

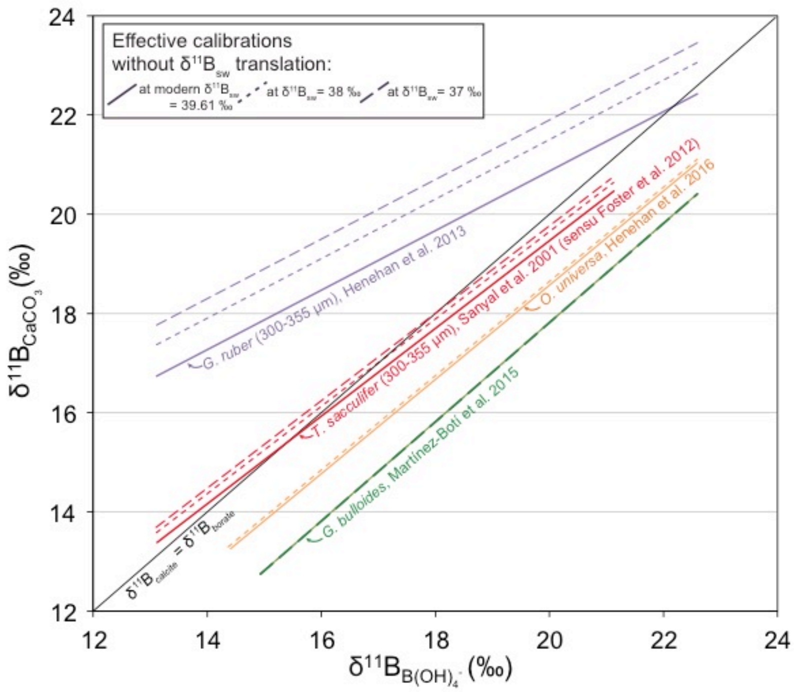

Figure S1: Boron isotope calibration lines at three different $\delta^{11}B_{sw}$. Data increasingly suggest that both elevated values of $\delta^{11}B$ and lowered *pH-sensitivity* in some species (e.g. *G. ruber, T. sacculifer*) derive from symbiont photosynthesis. In these species, the magnitude of relative microenvironment pH elevation, and hence the offset between $\delta^{11}B_{borate}$ and $\delta^{11}B_{calcite}$, increases as ambient pH decreases- as described in modern $\delta^{11}B_{calcite}$-$\delta^{11}B_{borate}$ calibrations by the slope of the calibration line (shown here as solid lines). When applying these modern calibrations in the past, however, these calibration lines will conflate two sources of variation in foraminiferal $\delta^{11}B$: seawater pH and changing $\delta^{11}B_{sw}$. Effectively, in an ocean with lower $\delta^{11}B_{sw}$ (and hence lower $\delta^{11}B_{calcite}$) but pH ≈ modern, a modern *G. ruber* or *T. sacculifer* calibration will over-correct $\delta^{11}B_{calcite}$ for microenvironment pH vital effects, because it assumes that lower measured $\delta^{11}B_{calcite}$ is solely a product of lowered ambient pH (at which vital effects should be greater). As is shown, for *O. universa* (orange lines; *Henehan et al.,* (2016)) and *G. bulloides* (green lines; Martínez-Botí et al., (2015)), where pH-sensitivity is very close to that of aqueous borate ion, this has little effect. However, for shallower dwelling symbiont-bearing species with reduced pH sensitivity, such as *G. ruber* (purple lines; Henehan et al., (2013)) or *T. sacculifer* (red lines; Sanyal et al., (2001), Foster et al., (2012)) vital effects will be overstated. At a $\delta^{11}B_{sw}$ of 37 ‰, for example, boron isotope vital effect corrections in *T. sacculifer* would be inflated by 0.31 ‰, which at such low $\delta^{11}B_{sw}$ (where the sensitivity of the proxy is lower) could significantly bias palaeo-reconstructions toward lower pH and higher pCO_2. For *G. ruber*, a very low pH sensitivity, this problem is much greater. Note, the lines shown above were constructed by calculating microenvironment ΔpH suggested by modern calibrations for a given pH at different bulk $\delta^{11}B_{sw}$, and applying this ΔpH back to modern $\delta^{11}B_{sw}$ for comparison.

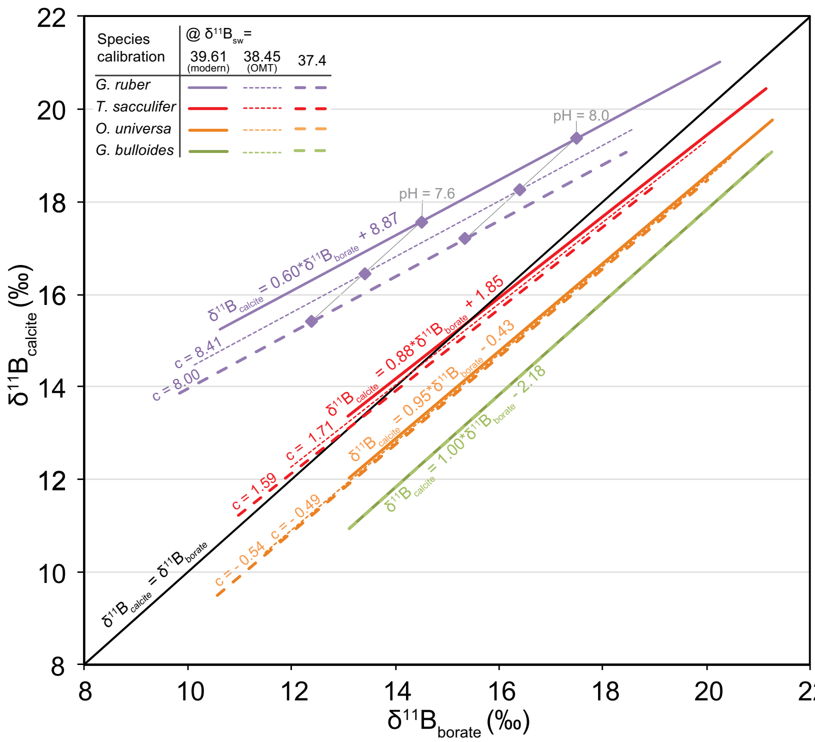

Figure S2: Translated modern calibrations for different values of past $\delta^{11}B_{sw}$. To address the issue described in Supplementary Figure 1, we plot the pH offsets in foraminiferal microenvironments implied by modern calibrations across the same range in ambient pH, but applied to seawater of differing $\delta^{11}B_{sw}$ (keeping pK^*_B constant) for *O. universa* (orange lines; *Henehan et al.,* (2016)), *G. bulloides* (green lines; Martínez-Botí et al., (2015)), *G. ruber* (purple lines; Henehan et al., (2013)) and *T. sacculifer* (red lines; Sanyal et al., (2001), sensu Foster et al., (2012)). For each calibration the slope (representing pH-sensitivity of $\delta^{11}B_{calcite}$) is unchanged, but the intercept, 'c', is shifted towards more negative values as $\delta^{11}B_{sw}$ is decreased (example values plotted). The intercept of calibrations with pH sensitivities lower than borate can be adjusted to account for this effect in future studies using the equation $c_{\delta^{11}B_{sw}} = c_0 +$

$\Delta\delta^{11}B_{sw}(m_0 - 1)$, where $c_{\delta^{11}B_{sw}}$ is the translated intercept at a desired $\delta^{11}B_{sw}$, c_0 and m_0 are the intercept and slope of the calibration at modern $\delta^{11}B_{sw}$, and $\Delta\delta^{11}B_{sw}$ is the difference in $\delta^{11}B_{sw}$ between modern $\delta^{11}B_{sw}$ and the $\delta^{11}B_{sw}$ of interest (i.e. modern $\delta^{11}B_{sw}$ minus the $\delta^{11}B_{sw}$ of interest).

.

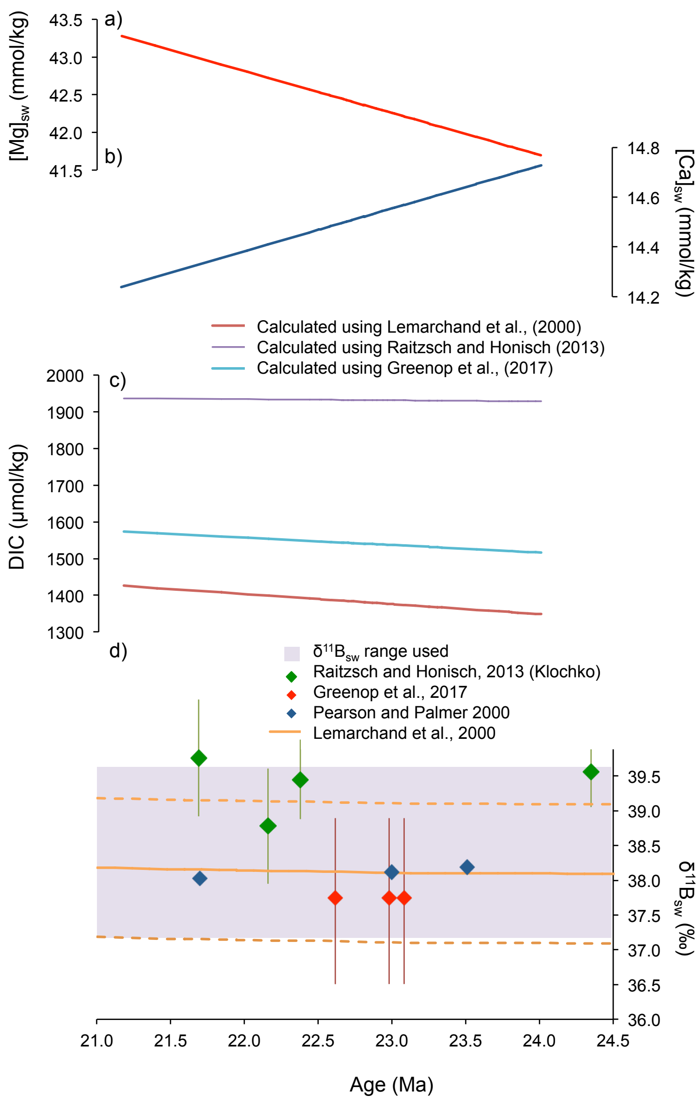

Figure S3: Input parameters into the δ^{11}B-pH calculations. (a) Mg and (b) Ca concentration of seawater based on a linear regression through the fluid inclusion data from Brennan et al., (2013) and Horita et al., (2002) following Sosdian et al., (2018). (c) The three DIC records used to calculate CO_2 from Sosdian et al., (2018). Records are calculated using the $\delta^{11}B_{sw}$ record of

Raitzsch and Hönisch, (2013) (purple line), Greenop et al., (2017) (blue line) and Lemarchand et al., (2000) (red line). (d) Composite of $\delta^{11}B_{sw}$ estimates across the OMT from Raitzsch and Hönisch, (2013) (green diamonds with 2σ error bars), Greenop et al., (2017) (red diamonds with 2σ error bars), Palmer et al., (1998); Pearson and Palmer, (2000) (blue diamonds) and Lemarchand et al., (2000) (solid orange line; dashed orange line is 2σ error). Purple shaded area is the range of $\delta^{11}B_{sw}$ used in this study. The minimum of this range is set to the lower 1σ uncertainty of the smoothed Greenop et al., (2017) record between 22.6 and 23.1 Ma and the maximum extent is determined by averaging the upper 1σ uncertainty of the $\delta^{11}B_{sw}$ estimates between 21.7 Ma and 24.4 Ma from Raitzsch and Hönisch, (2013).

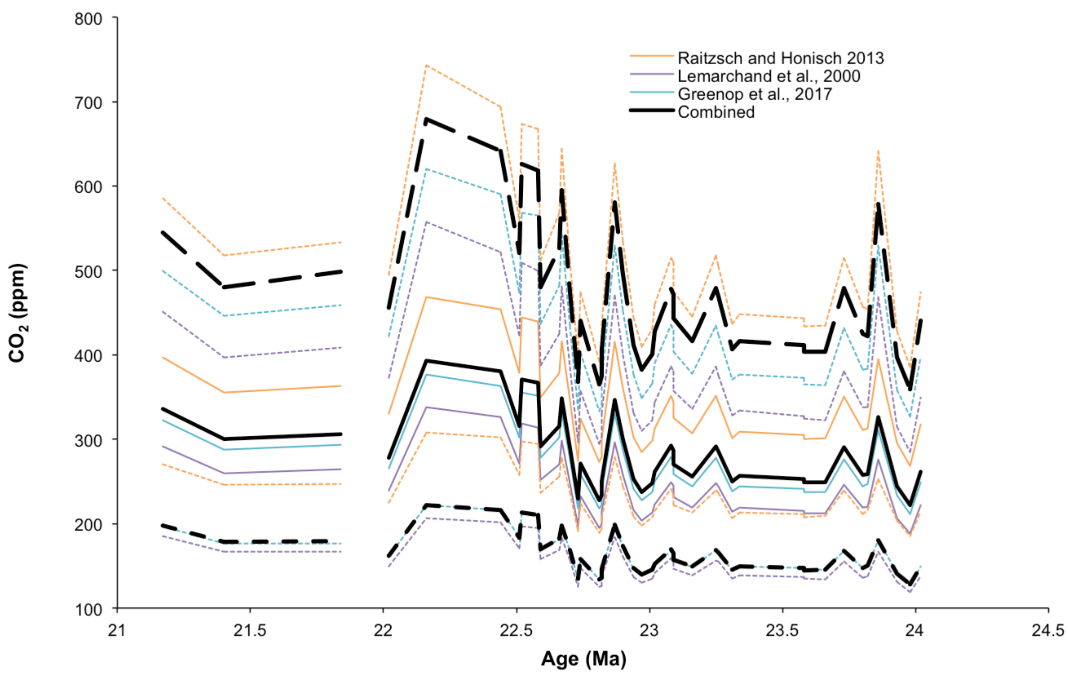

Figure S4: CO_2 calculated using the logDIC regressions from Sosdian et al., (2018) calculated with Raitzsch and Hönisch, (2013) (solid orange line; dashed orange line is 2σ error), Greenop et al., (2017) (solid blue line; dashed blue line is 2σ error) and Lemarchand et al., (2000) (solid purple line; dashed purple line is 2σ error). Black line is the median (solid line) and 2σ (dotted line) of the combined Monte Carlo simulations of CO_2 calculated using the three different logDIC regressions (n=30000).

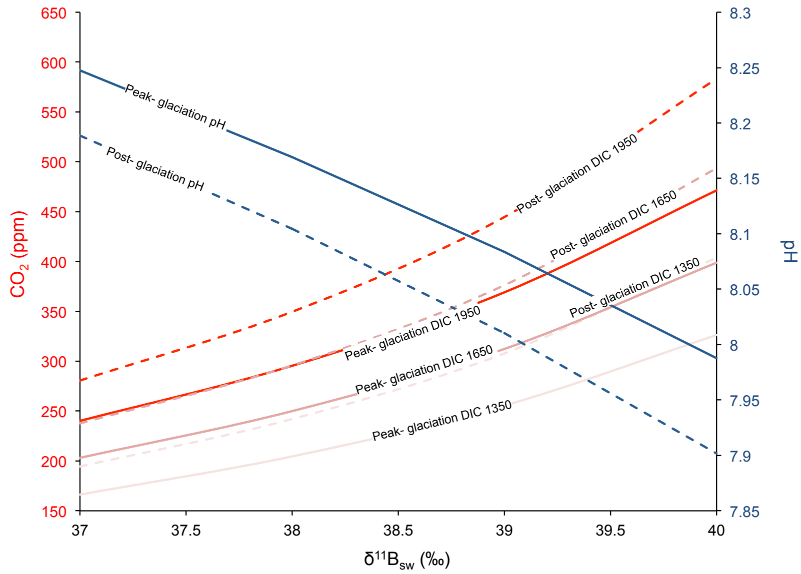

Figure S5: Sensitivity of pH and CO_2 to estimated $\delta^{11}B_{sw}$ and DIC. Blue line shows reconstructed pH for post- (dashed line) and peak- (solid line) OMT (as defined in Fig. 5a) as a function of $\delta^{11}B_{sw.}$ CO_2 is calculated at DIC 1350 µmol/kg (light pink), DIC 1650 µmol/kg (dark pink) and 1950 µmol/kg (red) for peak OMT (solid line) and post OMT (dashed line) with varying $\delta^{11}B_{sw.}$

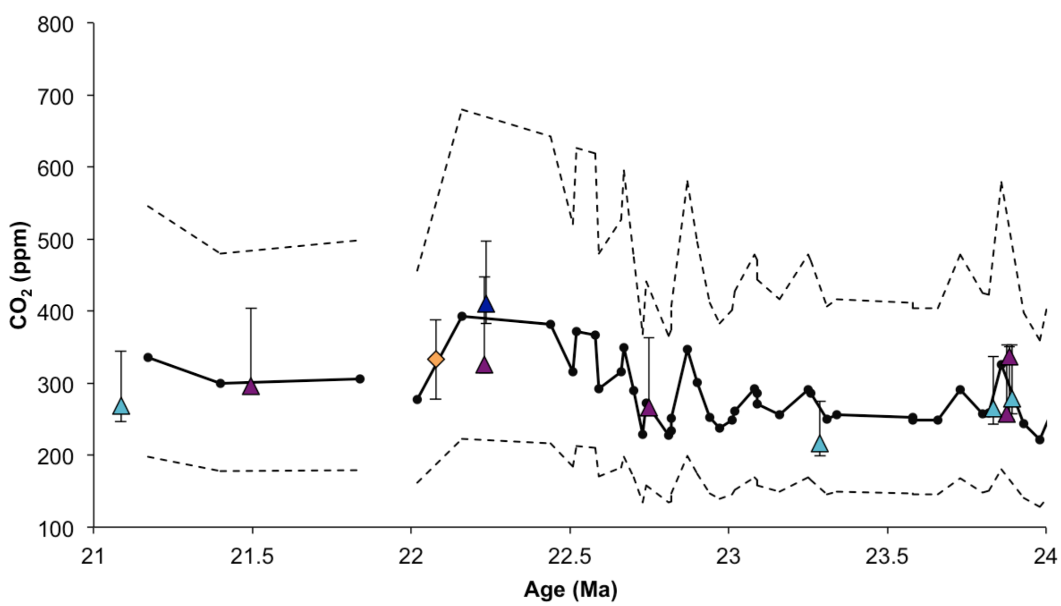

Figure S6: New CO_2 record from this study (black line and circles) with median (solid line) and 2σ (dotted line) uncertainty. The uncertainty is fully propagated using a Monte Carlo simulation (n=30000) and including uncertainty on temperature, salinity, the DIC relationship, $\delta^{11}B_{sw}$ and the $\delta^{11}B$ measurement. Also plotted are previously published CO_2 records from across the OMT glaciation. Alkenone reconstructions (light blue and purple) from Pagani et al., (2005) and (dark blue) from Zhang et al., (2013) plotted on the age model of Pagani et al., (2011) updated to Gradstein et al., (2012). Leaf stomata CO_2 reconstruction (yellow diamond) from (Kürschner et al., 2008).

Data Set S1: $\delta^{11}B$ and Mg/Ca data from ODP Site 926 and ODP Site 872 (from Greenop et al., 2017 and this study) with estimates of CO_2/SST (this study) and $\delta^{18}O_{sw}$ (from Mawbey and Lear, 2013). Sample information (Columns A-F) includes Site, Core, Section, Interval, Depth (mcd) and Age. Age models for Site 926 and Site 872 are from Pälike et al., (2006a) (and references therein) and Sosdian et al., (2018) updated to GTS2012 (Gradstein et al., 2012) respectively. Mg/Ca data (Column G) and $\delta^{11}B$ data and uncertainties from 2 replicates and averaged (Columns H-M). Published $\delta^{18}O_{sw}$ from Mawbey and Lear, 2013 (Column N). Calculated SSTs (Column O) and CO_2 with associated uncertainties (Columns P-T). See main text for details of CO_2 and SST calculation.